Micro and Nanostructured Surfaces for Enhanced Phase Change Heat Transfer

by

Kuang-Han Chu

SUBMITTED TO THE DEPARTMENT OF MECHANICAL ENGINEERING IN PARTIAL FULFILLMENT OF THE REQUIREMENTS FOR THE DEGREE OF

Ph.D. in Mechanical Engineering
AT THE
MASSACHUSETTS INSTITUTE OF TECHNOLOGY

January 2013
[FEBRUARY 2013]

Signature of Author:_____
Department of Mechanical Engineering
January 15, 2013

Certified by:_____
Evelyn N. Wang
Associate Professor of Mechanical Engineering
Thesis Supervisor

Accepted by:_____
David Hardt
Professor of Mechanical Engineering
Chairman, Graduate Thesis Committee

To my dear parents

Micro and Nanostructured Surfaces for Enhanced Phase Change Heat Transfer

By

Kuang-Han chu

Submitted to the Department of Mechanical Engineering
On Jan. 15th, 2013 in partial fulfillment of the
Requirements for the Degree of Ph.D. in
Mechanical Engineering

Abstract

Two-phase microchannel heat sinks are of significant interest for thermal management applications, where the latent heat of vaporization offers an efficient method to dissipate large heat fluxes in a compact device. However, a significant challenge for the implementation of microchannel heat sinks is associated with flow instabilities due to insufficient bubble removal, leading to liquid dry-out which severely limits the heat removal efficiency. To address this challenge, we propose to incorporate micro/nanostructures to stabilize and enhance two-phase microchannel flows. Towards this goal, this thesis focuses on fundamental understanding of micro/nanostructures to manipulate liquid and vapor bubble dynamics, and to improve overall microchannel heat transfer performance.

We first investigated the role of micro/nanostructure geometry on liquid transport behavior. We designed and fabricated asymmetric nanostructured surfaces where nanopillars are deflected with angles ranging from 7°-52°. Uni-directional liquid spreading was demonstrated where the liquid propagates in a single preferred direction and pins in all others. Through experiments and modeling, we determined that the spreading characteristic is dependent on the degree of nanostructure asymmetry, height-to-spacing ratio of the nanostructures, and intrinsic contact angle. The theory, based on an energy argument, provides excellent agreement with experimental data. This work shows a promising method to manipulate liquid spreading with structured surfaces, which potentially can also be used to manipulate vapor bubble dynamics.

We subsequently investigated the effect of micro/nanostructured surface design on vapor bubble dynamics and pool boiling heat transfer. We fabricated micro-, nano-, and hierarchically-structured surfaces with a wide range of well-defined surface roughness factors and measured the heat transfer characteristics. The maximum critical heat flux (CHF) was ~250 W/cm^2 with a roughness factor of ~13.3. We also developed a force-balance based model, which shows excellent agreement with the experiments. The results demonstrate the significant effect of surface roughness at capillary length scales on enhancing CHF. This work is an important step towards demonstrating the promising role of surface design for enhanced two-phase heat transfer.

Finally, we investigated the heat transfer performance of microstructured surfaces incorporated in microchannel devices with integrated heaters and temperature sensors. We fabricated silicon micropillars with heights of 25 μm, diameters of 5-10 μm and spacings of 5-10 μm in microchannels of 500 μm × 500 μm. We characterized the performance of the microchannels with a custom closed loop test setup.

This thesis provides improved fundamental understanding of the role of micro/nanostructures on liquid spreading and bubble dynamics as well as the practical implementation of such structures in microchannels for enhanced heat transfer. This work serves as an important step towards realizing high flux two-phase microchannel heat sinks for various thermal management applications.

Thesis Committee Chair:

Prof. Evelyn N. Wang, Department of Mechanical Engineering, MIT

Thesis Committee Members:

Prof. Gareth H. McKinley, Department of Mechanical Engineering, MIT
Prof. John H. Lienhard, Department of Mechanical Engineering, MIT

Acknowledgements

First, I sincerely thank my thesis advisor, Professor Evelyn Wang, for introducing me to the field of thermal and heat transfer science. In these years, Evelyn has always been supportive of my research. Her continuous encouragement and enthusiasm for new discovery is one of the main driving forces to lead me through my study at MIT. She is also a kind person and great teacher. She cares about not only the research but also the education and shows consideration for students' life and future. I am truly grateful having her as my Ph.D. mentor.

I wish to thank my thesis committee members, Professors John Lienhard and Gareth McKinley, for their valuable advices and insightful guidance on the work presented herein, and their encouragement for my study.

I would like to thank our former postdoctoral associate, Dr. Ryan Enright, for his tremendous help during my Ph.D study. Ryan is one of the best researcher I have ever met. His creative ideas, unstoppable passion, and dedication to scientific research have inspired me to keep working on my study when I was at my low pointes. I feel grateful to have him work with me.

I also thank my master advisor, Professor Cheng-Hsien Liu for being supportive of the idea of me studying abroad. He led me into the scientific research and inspired my interest in micro/nanotechnology. I really appreciate his help.

Special thanks to all the members in DRL. Thank you all for the support and help. I wish you all the best of luck in your future endeavors.

I wish to offer special thanks to my friends: Andrew Koo, Rong Xiao, Michael Chang, Cheng-Hsun Wu, Lisa Kang, and Kammy Yang. Thank you for helping me enduring many challenges and difficulties during my study at MIT.

Finally, I give my thanks and appreciations to my parents, for their unconditional support and love through my studies. I hope they can feel proud for my achievements. I gratefully dedicate this thesis to my parents.

Studying at MIT and working at the Device Research Lab (DRL) for almost 6 years was an amazing experience. As the first group of students in DRL, I feel fortunate to see the group grow from the very beginning. I still remember the group meetings in my first year when there were only four people, the moment when the first optic tables was set up in 7-021, the first microscope we bought, the first experiment we conducted, and many firsts. I also remember the surprise we had when we first made the asymmetric nanopillars, the joy we got when we saw the movement of the magnetic nanopillars, and, of course, the excitement we felt when the first time we observed the uni-directional liquid spreading. Time goes by so quickly and DRL has grown to such a big group. I feel grateful to be a part of the DRL history and wish her all the best in the future.

Table of Content

Chapter 1 Background and Introduction

1.1 Micro-Electro-Mechanical Systems

Microelectromechanical systems (MEMS) are small integrated devices or systems that combine electrical and mechanical components, ranging in size from the submicrometer (or sub micron) level to the millimeter level. Due to the great potential [1] and broad applications of microscale systems, MEMS has experienced significant growth in the past decades. For example, the digital micromirror device (DMD), where arrays of millions of MEMS-based micromirrors, on a chip the size of a dime and are each independently addressable and drivable, reflect light to produce the images projected on TV screens or classroom walls [2] and MEMS accelerometers and gyroscopes provide the possibility of intuitive motion controls for mobile devices or gaming platforms [3].

An emerging research topic of MEMS is micro/nanostructure engineering on surfaces. The structured surfaces have long been recognized for being able to magnify the intrinsic wetting properties to achieve superhydrophilic or superhydrophobic surfaces in combination with chemical modifications [4-6]. Such capability has great potential in a wide range of applications including DNA microarrays, digital lab-on-a-chip, anti-fogging and fog-harvesting, inkjet printing and drag-reduction [7-13]. In addition to the rich opportunity in manipulation of fluid dynamics, there has been a growing realization that the micro/nanostructured surfaces can enhance heat transfer performance of phase change processes, which is of interest because of the applications in thermal management and power generation [14].

1.2 Challenge in Thermal Management

Fast increasing processing capacity within the size confines of modern integrated circuits (ICs) has made thermal management a key barrier to the continued development and progress of new electronic devices. One example is the Central Processing Unit (CPU). As shown in Fig. 1-1 (adapted from [15]), from the early 90's to 2005, the power density of CPUs steadily increased to 100 W/cm^2. Since then, typical commercialized thermal management approaches has not been able to dissipate such high fluxes and the industry adopted novel designs such as "multi-core" to reduce the heat flux. However, John Thome, in a 2006 editorial, suggested that ICs may require over 300 W/cm^2 of power removal in the next few years [16]. In addition, the thermal management demands of specialty applications such as concentrated photovoltaics, power electronics, and laser diode are even more severe, requiring power densities of over 1000 W/cm^2 [17-19]. In addition to the high heat flux, the strong effect of temperature on the efficiency requires the thermal management schemes capable of dissipating high heat fluxes with low temperature rises, *i.e.,* narrow temperature budget. To help realize the desired performance of future electronic devices, new and innovative technologies for heat dissipation need to be developed.

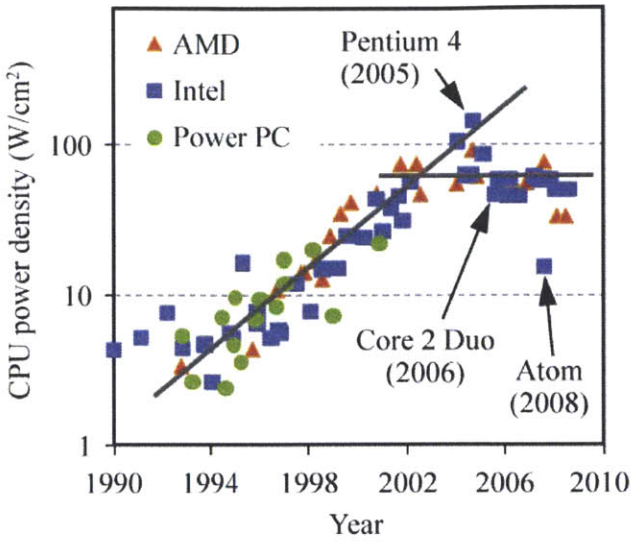

Figure 1-1. Recent trend in power density of CPUs. Heat fluxes as high as 100 W/cm^2 has been a major bottleneck for increasing integration level. (Adapted from [15])

1.3 Cooling Schemes Based on Phase Change

While forced air cooling in conjunction with integrated heat pipes are typically limited to dissipating ~100 W/cm^2, phase change based cooling techniques, such as pool boiling, spray cooling and flow boiling, have the potential to remove heat flux on the order of 100-1000 W/cm^2, as shown in Fig. 1-2 [20] due to latent heat of vaporization. Therefore, two-phase cooling is considered as one of the most promising method to address those thermal management needs.

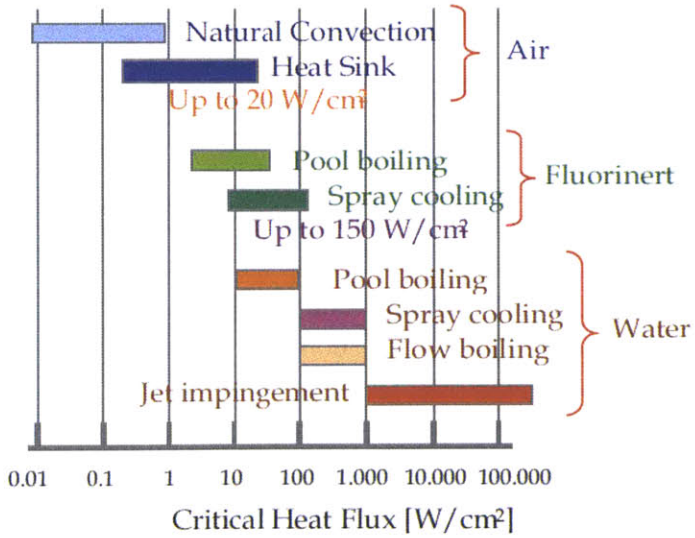

Figure 1-2. Comparison of critical heat flux (CHF) with different cooling schemes. Phase change based cooling techniques using water as working fluid promises the highest heat dissipation capability. (Adapted from [20])

1.3.1 Critical Heat Flux

In two-phase (boiling) heat transfer systems, the critical heat flux (CHF) represents the operational limit of heat flux because the transition from nucleate boiling to film boiling occurs when the heat flux is above CHF. In film boiling, the formation of a vapor film covers the heating surface completely and loss of contact between the surface and liquid leads to a significant rise in thermal resistance and, as a result, reduction in heat transfer efficiency. Due to much practical interest, the mechanism that causes CHF has been intensively studied, for example, Kelvin–Helmholtz instability due to the high relative velocity between the liquid layer and vapor emanating from columns [21, 22], merging of vapor columns to produce a vapor blanket [23], dry-out of the liquid macrolayer [24, 25] and hot/dry spot re-wetting [26, 27]. However, the detailed mechanism for CHF is still under debate and investigation [28].

1.3.2 Pool Boiling

Pool boiling is considered one of the simplest methods to achieve heat fluxes over 100 W/cm^2 with passive method which doesn't require extra power input. Therefore, a variety of models have been proposed on predicting the maximum CHF limit in pool boiling, such as the classic hydrodynamic model proposed by Zuber [21], models based on capillary pumping limit and viscous drag [29, 30], Kandlikar's model based on the dynamics of vapor bubble expansion [26], and the model based on the macrolayer hypothesis [31]. However, the maximum heat flux of pool boiling is lower than other two-phase cooling methods due to the passive liquid supply. Furthermore, pool boiling usually has a high working temperature and is sensitive to orientation, which limits application in thermal management for electronic devices.

1.3.3 Spray Cooling

Spray cooling utilizes liquid droplets to impinge on the hot surface and form a very thin liquid layer. The evaporation of the thin layer removes a large amount of heat. Lin and Ponnappan reported a maximum heat flux of 500 W/cm^2 with a water spray from eight nozzles [32]. However, an ultra high pressure (hundreds of kPa) is required to create spray flow, which can hardly be allowed in commercial packages. Researchers have also proposed using piezoelectric vibrators or inkjet printer technology to create sprays [33]. In addition to the ultra high pressure and power needed, another concern about spray cooling is the intricate flow patterns. Hall and Mudawar reported that identical spray nozzles from the same production batch failed to create identical spray flows [34].

1.3.4 Flow Boiling

Forced flow boiling in channels allows for extremely high heat removal rates by utilizing the latent heat of vaporization of a liquid. The result is that a significantly lower mass flow rate is needed to cool a chip when compared to forced liquid-phase flow, and a more constant temperature can be maintained across the entirety of the chip [35]. Two-phase microchannel heat

sinks offer significant advantages over macroscale solutions because the high surface area to volume ratios in these devices allows for more efficient heat removal rates at low vapor qualities, which is contrary to results seen in the macroscale case [36-38]. Thermal resistances of less than 0.1 K/W can be achieved using two-phase flows within microchannels and their small footprint makes their use ideal [39]. For example, Penley and Wirtz demonstrated a heat flux of up to 446 W/cm^2 with water using copper filament screen laminates to enhance surface area in microchannels [40].

1.4 Challenges in Flow Boiling

While flow boiling in microchannels has demonstrated promising potential for high flux cooling, the practical implementation of microchannel heat sinks presents additional challenges and hurdles. In large piping systems, the regimes associated with two-phase flows have been extensively studied. As the vapor quality within the pipe increases, the system moves from bubbly flow to slug flow and, eventually, to an annular or stratified flow, as shown in Figure 1-3 [41]. Surface tension forces are insignificant compared to inertial forces while the characteristic length of the pipeline is at least an order of magnitude larger than capillary length, *i.e.*, ~2 mm for clean water. Buoyancy and lift forces play important role at this scale and, therefore, can be utilized through proper design to stabilize the multiphase flow systems [42].

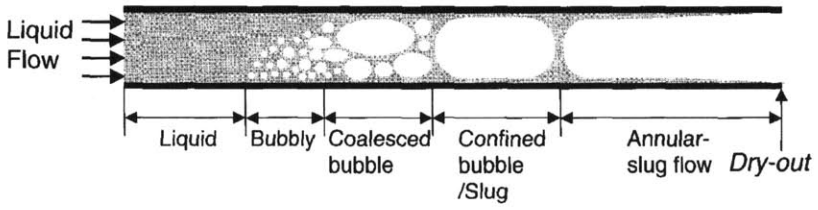

Figure 1-3. Illustration of two-phase flow patterns occurring in a macroscale evaporator pipe. As the liquid flows from left to right along the heating pipeline, it moves from bubbly flow to slug flow to annular flow. (Adapted from [41])

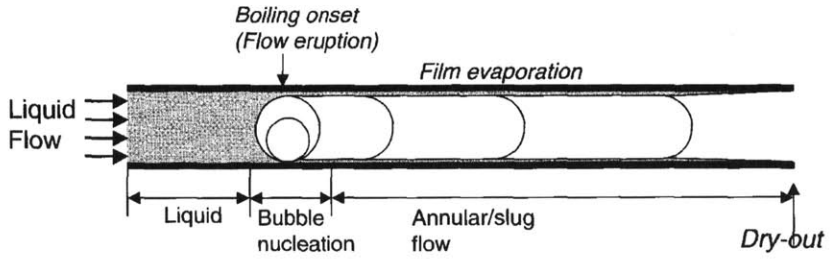

Figure 1-4. Flow regimes in a two-phase microscale pipe. As the onset nucleation occurs, the vapor bubble expands rapidly and the flow pattern moves quickly from slug flow to annular flow and, eventually, to dry-out. (Adapted from [43])

In two-phase microfluidics, however, the buoyancy and lift forces are insignificant, while surface tension forces dominate inertial effects leading to insufficient bubble removal. The rapidly expanding bubbles in microchannels where the fluid undergoes boiling causes high pressure drops and flow reversals developed in the channel, leading to large pressure fluctuations and flow instabilities [42-48]. As a result, two-phase flows within microchannels quickly reach the slug flow regime, and annular flow and dry-out occur rapidly, as shown in Figure 1-4 [43]. These vapor slugs result in high pressure drops and a significant loss in liquid-surface contact area over the length of the channel, which significantly lowers the cooling efficiency of the system.

1.5 Micro/Nanostructure in Two-Phase Microchannel Heat Sink

1.5.1 Flow Constrictor and Microcavity

To address the problem of flow instability in two-phase microchannel heat sinks and to increase the maximum heat flux, a special constrictor has been proposed to be integrated into the channel entrance to help control the backflow and reduce the pressure fluctuations. For example, Koşar *et al.* achieved heat flux as high as 614 W/cm^2 by water flow boiling in microchannels with restrictors at the entrance to stabilize the flow [49].

Another approach to suppress the instability during flow boiling is to enhance bubble nucleation at low wall superheats using artificial nucleation sites [50, 51]. At onset of nucleation boiling (ONB), the maximum pressure that can be sustained inside the vapor bubble is dictated by the saturation pressure corresponding to the heater surface temperature [52]. Therefore, the reversed flow and flow instabilities developed due to high pressure inside bubble are suppressed when local superheat at ONB is reduced by making nucleation sites available on the heating surface. A maximum heat flux of 445 W/cm^2 has been demonstrated using water in the microchannels with a hydraulic diameter of 227 μm possessing 7.5 μm wide reentrant cavities on the sidewalls [51].

While most studies on flow instability mitigation in two-phase microchannel heat sinks are focused on using structured surface to modulate inlet pressure [49, 50], increase surface area [53-55], and promote bubble nucleation [51, 56], these approaches either suffer from high overall system pressure drop [49, 50, 53-55], or limited enhancements in heat transfer after ONB [57]. The problem of insufficient bubble removal in two-phase microchannel has never been fully addressed. The approach to manipulate bubble dynamics for flow boiling has not been investigated due to the complexity of two-phase flow [26]. Therefore, two-phase microchannel heat sinks are still far from practical implementation.

1.5.2 Micro/Nanopillar Arrays

It has been shown that surface structures and wettability can affect the bubble dynamics, including bubble departure radius and frequency [58, 59]. In recent years, there is a growing

consensus that surface wettability plays an important role in defining the heat transfer performance due to the capability to manipulate bubble behaviors [26, 30], and the significant enhancements in CHF of pool boiling that have been demonstrated using superhydrophilic micro/nanostructured surfaces [60-64]. In the microchannels, there is also evidence that surface wettability can affect bubble dynamics [65]. As discussed previously, the wetting property is greatly augmented on the surfaces with micro/nanostructures. Therefore, the micro/nanostructured surface (*i.e.*, micro/nanopillar array on surface) provides a great potential to manipulate bubble dynamics to promote bubble departure. Furthermore, the micro/nanopillar array can both increase nucleation site density and provide a wide range of size of nucleation sites, where vapor bubble nucleation is triggered at different wall superheat based on cavity diameters [66]. Thus, the overall heat transfer performance is significantly enhanced [60, 67].

1.6 Scope of the Thesis

This thesis aims at improving fundamental understanding in bubble dynamics on micro/nanostructured surfaces, investigating methods to promote bubble departure, and demonstrating practical enhancements for two-phase microchannel heat sinks.

In Chapter 2 of this thesis, the dynamics of liquid spreading in nanopillar arrays is first investigated and a uni-directional liquid spreading, where liquid propagates in a single preferred direction and pins in all others, on a special designed, asymmetric nanostructured surfaces will be presented. A theory, based on an energy argument, is developed to predict the spreading behaviors and shows an excellent agreement with experimental results. This work shows that we can manipulate droplet spreading to a single direction on-demand, which suggests new opportunities to tailor advanced nanostructures to achieve active control of complex flow patterns, which potentially can affect vapor bubble to grow and departure in a preferred direction.

In Chapter 3, the effect of surface roughness-augmented wettability on pool boiling heat transfer is studied. Micro/nanostructured surfaces with a wide range of well-defined surface roughness were fabricated and a maximum CHF of ~208 W/cm^2 was achieved with a surface roughness of ~6. An analytical force-balance model was extended to explain the CHF enhancement. The excellent agreement found between the model and experimental data supports the idea that roughness-amplified capillary forces are responsible for CHF enhancement on structured surfaces. This work is an important step towards demonstrating the promising role of surface design for manipulating bubble dynamics. The insights gained from this work suggest design guidelines for new surface technologies with high heat removal capability.

A large enhancement in critical heat flux (CHF) on hierarchically-structured surfaces fabricated using electrophoretic deposition on microstructured silicon and electroplated and oxidized copper is reported in Chapter 4. A CHF of ~250 W/cm^2 was achieved on the CuO hierarchical surface with a surface roughness factor of ~13.3. Compared to the CHF model

proposed, the excellent agreement found between the model and experimental data supports the idea that roughness-amplified capillary forces are responsible for CHF enhancement on structured surfaces and demonstrates the validity of the model for roughness ratio ranging from 1 to ~15. This work provides design guidelines for new surface technologies with higher heat removal capability that can be effectively used by industry.

Heat transfer performance of microstructured surfaces integrated into microchannel devices with heaters and temperature sensors is demonstrated in Chapter 5. The fabricated silicon micropillars have heights of 25 μm, diameters of 5-10 μm and spacings of 5-10 μm in the microchannels of 500 μm × 500 μm. We characterized the performance of the microchannels with a custom closed loop test setup. The preliminary data shows the device is capable to dissipate heat flux of ~508 W/cm^2 with mass flux of ~1530 kg/m^2 s.

Chapter 2 Manipulation of Liquid Spreading using Structured Surfaces

2.1 Introduction

Controlling surface wettability and liquid spreading on patterned surfaces is of significant interest for a broad range of applications, including DNA microarrays, digital lab-on-a-chip, anti-fogging and fog-harvesting, inkjet printing, and thin film lubrication [7-10, 13, 68-70]. Advancements in surface engineering, with the fabrication of various micro/nanoscale topographic features [11, 71-74], and selective chemical patterning on surfaces [75, 76], have enhanced surface wettability [4, 68, 77], and enabled control of the liquid film thickness [78] and final wetted shape [79]. In addition, groove geometries and patterned surface chemistries have produced anisotropic wetting, where contact angle variations in different directions resulted in elongated droplet shapes [80-86]. In all of these studies, however, the wetting behavior preserves left-right symmetry. Here, we demonstrate that we can harness the design of asymmetric nanostructured surfaces to achieve uni-directional liquid spreading, where the liquid propagates in a single preferred direction and pins in all others. Through experiments and modeling, we determined that the spreading characteristic is dependent on the degree of nanostructure asymmetry, height-to-spacing ratio of the nanostructures, and intrinsic contact angle. The theory, based on an energy argument, provides excellent agreement with experimental data. The insights gained from this work offer new opportunities to tailor advanced nanostructures to achieve active control of complex flow patterns and wetting on-demand.

2.2 Uni-Directional Liquid Spreading and Asymmetric Nanostructured Surfaces

When a droplet is deposited on a typical periodic nanostructured hydrophilic surface (Fig. 2-1**a** inset), the droplet shape is symmetric (Fig. 2-1**a**) and determined by a minimization of total surface energy. The incorporation of grooves or channel features [80-84], creates local energy barriers to pin the liquid along one axis and spread the liquid bi-directionally to form elongated droplets [84, 85]. Asymmetric nanostructures (Fig. 2-1**b** inset), on the other hand, can introduce energy barriers in more than one axis and allow the liquid to propagate in a single direction (Fig. 2-1**b**). This work investigates the design of asymmetric structures to achieve this unique behavior.

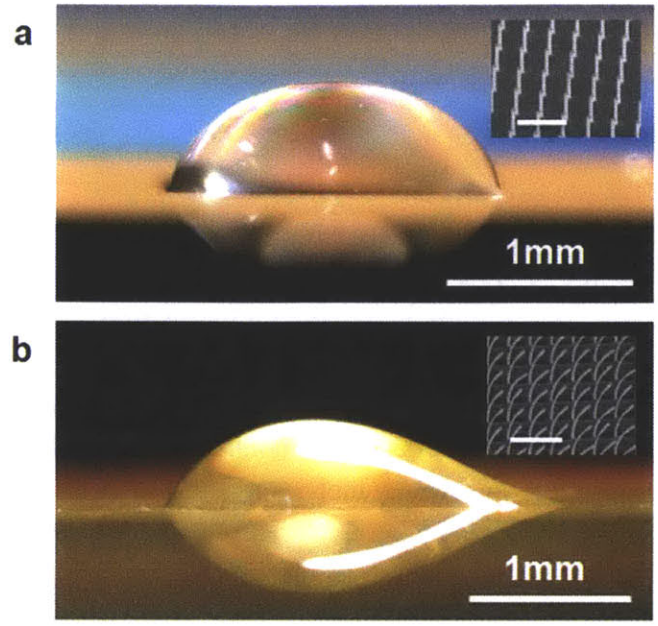

Figure 2-1. Comparison of wetting behavior on symmetric and asymmetric nanostructured surfaces. **a**, A 1 μL droplet of DI water with 0.002% by volume of surfactants (Triton X-100) deposited on typical vertical nanopillars with diameters of 500 nm, spacings of 3.5 μm, and heights of 10 μm (inset) with axially symmetric liquid spreading. **b**, A droplet on the same dimension nanostructures as **a**, but with a 12° deflection angle (inset) with uni-directional liquid spreading. The images show the characteristics of a spreading droplet at one instant in time. The scale bars in the insets are 10 μm.

Asymmetric nanostructures were fabricated with pillar diameters ranging from 500-750 nm, heights of 6 and 10 μm, and spacings of 3.5 μm. The asymmetric nanopillar fabrication steps are described as follows. A 200 nm thick silicon dioxide (SiO_2) thin film was grown on a silicon wafer. The features were then defined *via* projection lithography with a thin photoresist (SPR700-1.0, Rohm and Haas Electronic Materials), and transferred onto the SiO_2 layer by plasma reactive ion etching (RIE). An oxygen plasma was used to remove residual photoresist and the remaining oxide layer was used as an etch protector. The pillars were etched in silicon using deep reactive ion etching (DRIE). The sample was subsequently placed in an electron beam evaporator chamber at tilt angles ranging from 18°-25° to deposit a thin gold film on one side of the pillars. During the deposition process, the gold was evaporated by an electron beam and then allowed to condense on the pillar surfaces. As a result, the gold film coated on the surface experienced a tensile stress. Meanwhile, the silicon pillars were heated by hot gold atoms which condensed on the surfaces. After the deposition process, nanostructures were cooled down to room temperature, which led to thermal residual stresses from the thermal expansion mismatch between the gold film and silicon pillars. The combination of the residual stresses allowed the nanopillars to deflect. While the temperature of the gold during the deposition

process is over 1000 °C, the temperatures in fluidic and biological applications are typically no larger than 100 °C. Therefore, the deflection angle of the nanopillars does not change under the temperature ranges of fluidic and biological applications. The thickness of the gold film was varied from 250 nm to 400 nm to obtain the desired deflection angles of 2°-52° (φ = 2°-52°). The fabricated pillars have actual heights of 6 μm (H = 6 μm) and 10 μm (H = 10 μm), and spacings of 3.5 μm (l = 3.5 μm), such that the height-to-spacing ratio is approximately 1.71 (H/l = 1.71) and 2.87 (H/l = 2.87), respectively. The diameters of the pillars range from 500-750 nm on different samples. The variation in pillar diameters is due to different thicknesses of deposited gold films to achieve the desired deflection angles. Figure 2-2 shows scanning electron micrographs (SEMs) of four representative asymmetric nanopillar arrays with deflection angles, φ, (defined in the Fig. 2-2 inset) ranging from 7°-52°. A Cartesian coordinate system is used for convenience, as shown in Fig. 2-2, where the pillars deflect in the positive X (+X) direction.

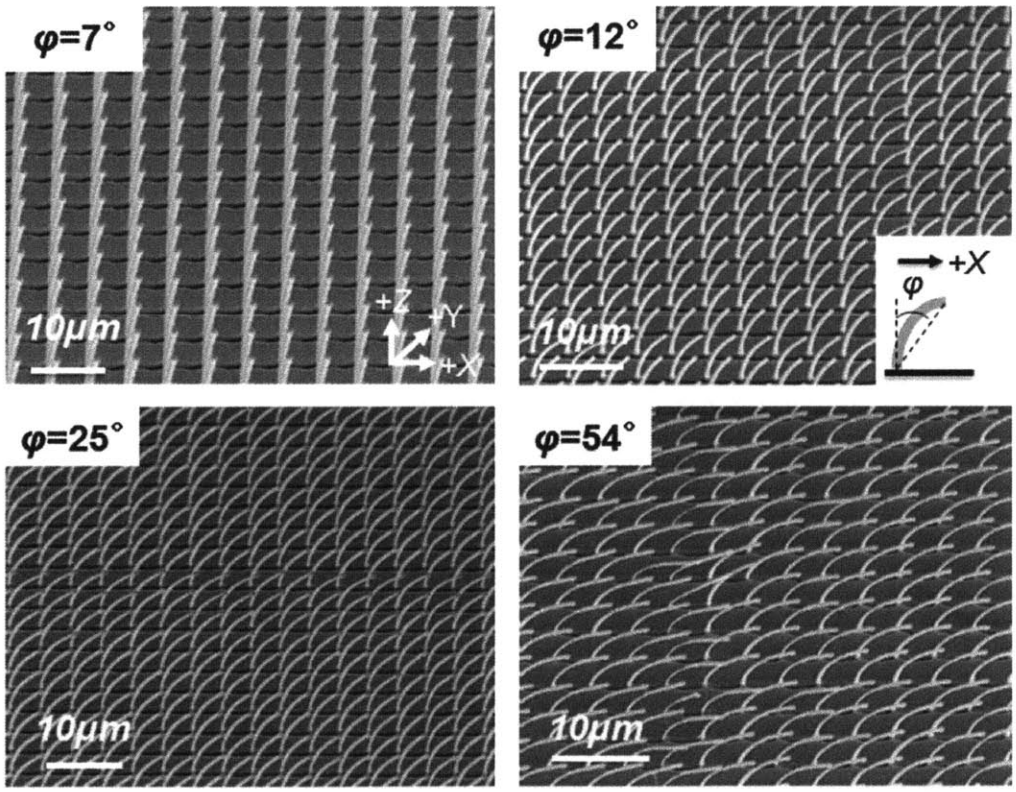

Figure 2-2. Scanning electron micrographs with uniform arrays of asymmetric nanostructured surfaces. The nanostructure deflection angles, φ, are 7°, 12°, 25°, and 52°. The diameters, spacings, and heights of the nanopillars are all 500-750 nm, 3.5 μm, and 10 μm, respectively. The Cartesian coordinate system is defined such that the pillars deflect in the positive X (+X) direction. While each surface has the same equilibrium contact angle (4°-8°, depending on the thickness of the gold film), the spreading behavior is dependent on the deflection angle. Inset: Schematic defining the deflection angle.

To investigate the effect of geometry on liquid spreading behavior, we conformally coated the nanopillars with a polymer using an initiated chemical vapor deposition (iCVD) process [87-89]. Initiated chemical vapor deposition (iCVD), developed by the Gleason Lab at MIT [87-89], offers a new, solvent-free technique to conformally deposit polymers on nanostructures. Monomer and thermally labile initiator vapors flow into a reactor with resistively heated filaments suspended above a deposition stage cooled by recirculating water to maintain substrate temperatures around room temperature. Depending on the initiator, the filaments are heated to 250 – 550 °C, which is hot enough to dissociate initiator molecules into radicals, while leaving the monomer molecules unaffected. The monomer and initiator radicals migrate to the chilled substrate where they undergo free radical polymerization to form the polymer film [88]. In our experiments, the nanostructured surfaces were coated with two kinds of polymers, p(n-isopropylacrylamide-co-di(ethylene glycol) divinylether) (p(NIPAAm-co-DEGDVE)) and p(cyclohexyl methacrylate-co-divinylbenzene) (p(CHMA-co-DVB)), to ensure that the surface properties are uniform and to control the surface energy. The intrinsic contact angles of DI water on 150 nm thick p(NIPAAm-co-DEGDVE) coated surfaces are 54° and 62°, depending on the extent of cross-linking of the polymer. The intrinsic contact angle of DI water on 100 nm thick p(CHMA-co-DVB) coated surfaces is 80°. Different polymers were used to tailor the surface energy such that the intrinsic contact angles are 54°, 62°, and 80° with deionized (DI) water.

2.3 Experimental Results

We performed spreading experiments with DI water and Dulbecco's phosphate buffered saline (DPBS, Sigma-Aldrich) on p(NIPAAm-co-DEGDVE) coated surfaces. DI water with surfactant (Triton X-100, Fisher Scientific) concentrations of 0.00125% to 0.01% by volume were used on p(CHMA-co-DVB) coated surfaces. The surface tension ranges from 42.6 to 30.2 dynes/cm, which corresponds to contact angles of 63° to 21° (see Fig. 2-3 and 2-4). In each experiment, a 1 μL droplet was deposited using a micropipette in contact to the surface to minimize spreading driven by inertia. Images of the spreading of the droplet were recorded using both a CMOS camera (Phantom V7, Vision Research) at a frame rate of 30 fps and a digital camera (EOS 50D, Canon) with a macrolens (MP-E 65 mm, Canon). To examine the liquid film in the nanostructures, a diffraction-limited white light microscope with a 100× magnification (NA=0.70) was used. Before and between experiments, the surfaces were cleaned with isopropyl alcohol and DI water to remove contaminants on the surfaces. In addition, the fabricated surfaces were robust and were used more than 50 times without any degradation and change in the spreading behavior.

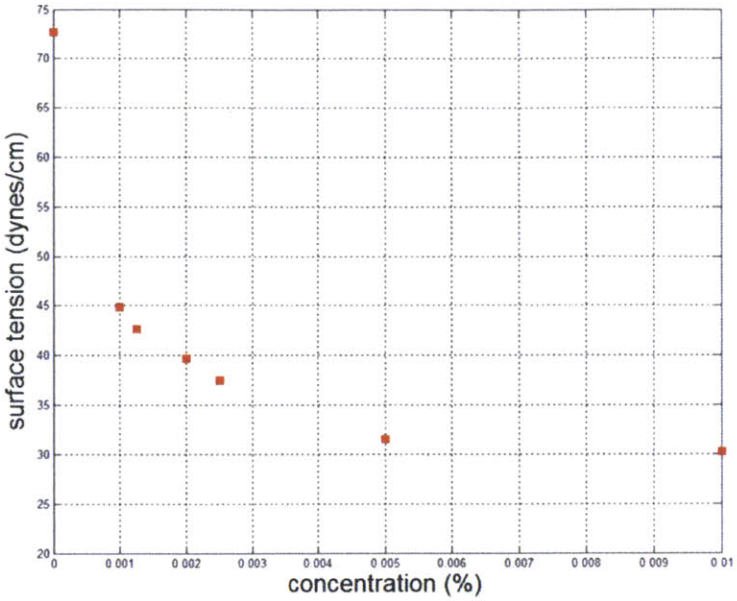

Figure 2-3. The surface tension with varying surfactant concentrations. The surface tension with increasing surfactant (Triton X-100) concentrations was measured using a tensiometer (K11, KRŰSS). The critical micelle concentration (CMC) of Triton X-100 is approximately 0.01% by volume, which corresponds to a surface tension of 30.2 dynes/cm.

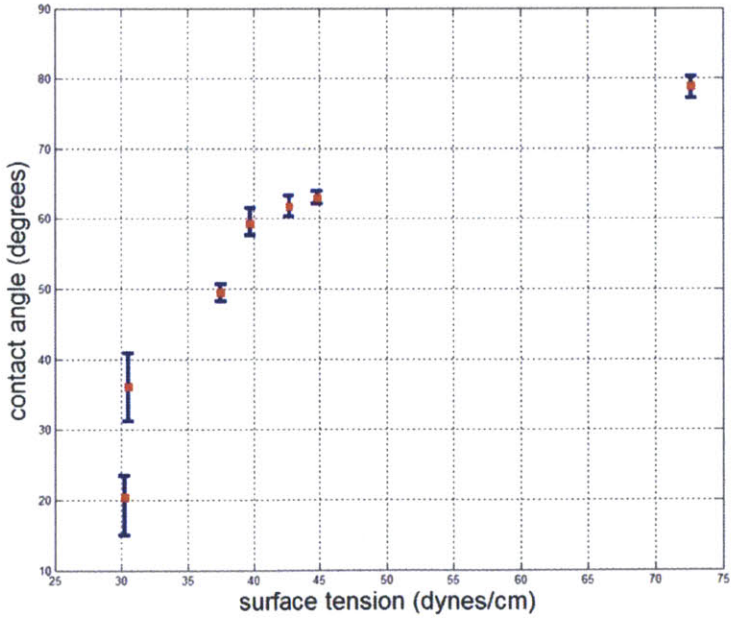

Figure 2-4. The contact angle with varying liquid surface tensions on the polymer, p(CHMA-co-DVB), coated flat surface. The contact angle decreases from 63° to 20.5° as the surface tension decreases from 42.6 to 30.2 dynes/cm. This relationship allowed studies of the spreading behavior with different contact angles on the nanostructured surfaces.

Typical uni-directional spreading behavior on the fabricated asymmetric nanostructures is shown with DI water and Dulbecco's phosphate buffered saline (DPBS) on surfaces where the deflection angle is 8.7° and the intrinsic contact angle is 62° (DI water). On another polymer coated surface with nanopillars deflected at 12° and an intrinsic contact angle of 80° (DI water), similar behavior is shown in the time-lapse images of the side and top view in Fig. 2-5**a** and 2-5**b**, respectively. In this particular case, DI water with a 0.002% concentration of surfactant (Triton X-100) by volume was deposited onto the surface where the intrinsic contact angle for this liquid (with a surface tension of 39.7 dynes/cm) is 59°. In all of these cases, the liquid propagates primarily in the +X direction while the contact line pins in both the –X direction and along the Y-axis. This uni-directional spreading associated with liquid pinning is distinct in comparison to previous studies [11, 72-74, 80-86] owing to the asymmetric geometry of the fabricated structures. The spreading behavior is independent of the initial droplet position, *i.e.*, for the same substrate and liquid, uni-directional spreading is observed when a droplet is placed at an arbitrary location on the surface. Furthermore, our experimental observations show that uni-directional spreading is determined by the nanopillar geometry and the intrinsic contact angle of the liquid on the polymer coated surface.

To elucidate the observed phenomena, we studied the liquid film propagating ahead of the droplet within the nanopillars, as indicated by the arrow in Fig. 2-5**b**. The behavior of the liquid film was found to be well-correlated with the behavior of the macroscopic droplet. We used white-light microscopy to investigate the effect of nanopillar deflection angle, φ, and the intrinsic contact angle, θ_{eq}, on liquid film propagation (see Methods section). DI water and DPBS were examined on the polymer coated surfaces (p(NIPPAm-co-DEGDVE)), where the intrinsic contact angles are 54° and 62° with DI water. To study the liquid behavior on a large range of deflection angles and intrinsic contact angles, we used DI water and DI water with surfactants (Triton X-100 with concentrations ranging from 0.01% to 0.00125% by volume) on another polymer (p(CHMA-co-DVB)) coated surface with an intrinsic contact angle of 80° (DI water). On this surface, surfactants were necessary to decrease the intrinsic contact angle in order to satisfy the condition for imbibitions [72].

The experimental results in Fig. 2-6 indicate the regimes in which the liquid propagates and pins in both the +X and –X directions for nanopillar heights of 10 μm (see Fig. 2-7 for additional experimental results with nanopillar heights of 6 μm). The square symbols (□) indicate experiments in which the liquid film propagates only in the +X direction, whereas the circles (○) are experiments where the film propagates in both +X and –X. The triangles (Δ) show instances where the liquid film is nearly pinned in the –X direction, *i.e.*, the propagation rate was at least five times slower in –X than in +X. The crosses (×) represent experiments where the film does not propagate at all due to the imbibition condition. The behavior of the film along the Y-axis was similar to the behavior in the –X direction. The blue, red, and green colors of these symbols represent experiments with DI water, DI water with surfactants, and DPBS, respectively.

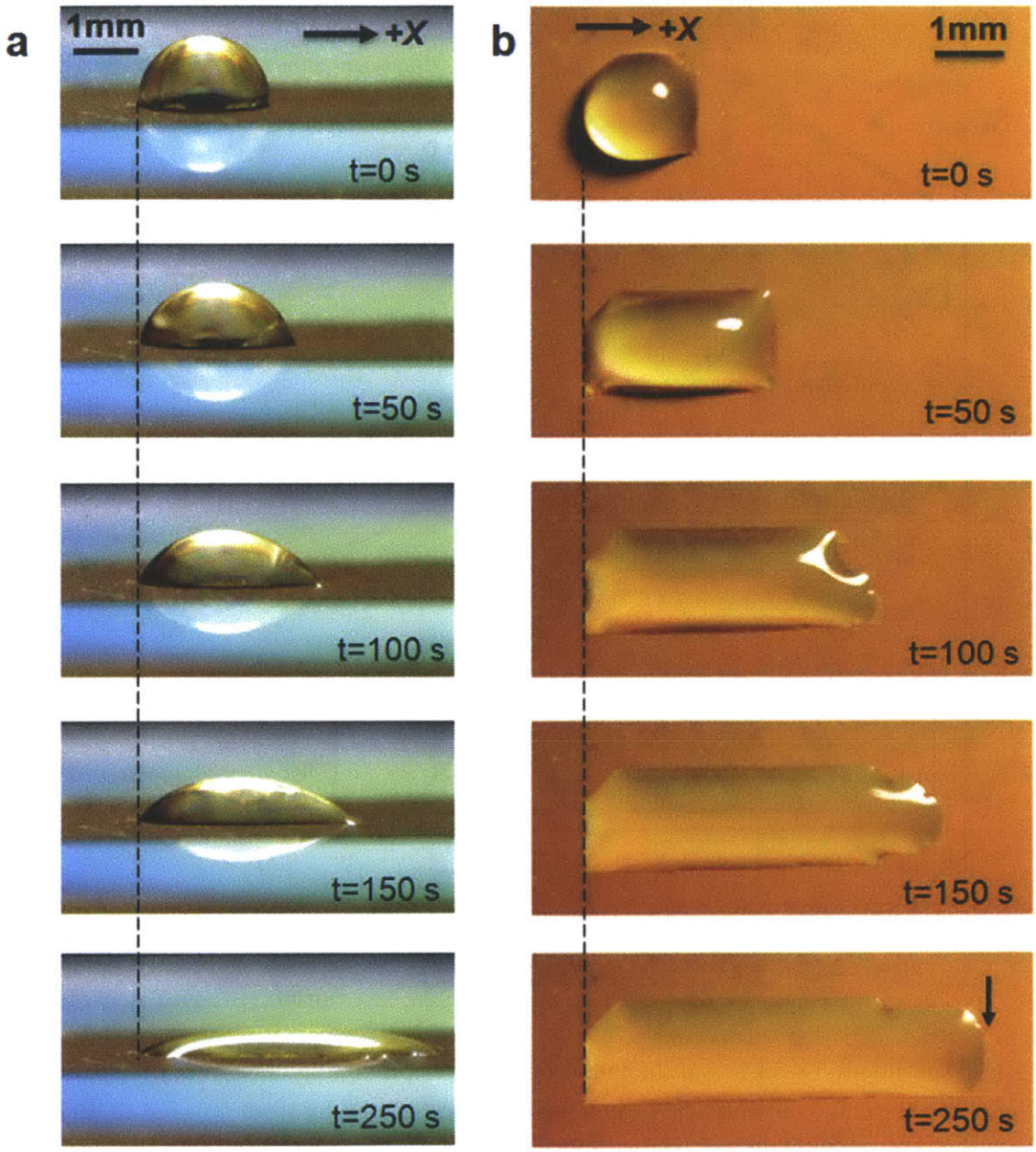

Figure 2-5. Time-lapse images of uni-directional spreading of a liquid droplet.
a, Side view and **b**, top view of a 1 μL droplet of DI water with 0.002% by volume of surfactant spreading on a surface with pillar diameters of 500 nm, spacings of 3.5 μm, and heights of 10 μm (with a height-to-spacing ratio of 2.87, H/l=2.87) deflected at 12° shown in Fig. 2-2. The initial location of the droplet contact line in the –X direction is indicated by the dotted lines, where the contact line stays pinned throughout the spreading process. A liquid film propagates ahead of the macroscopic droplet as highlighted by the arrow in **b**.

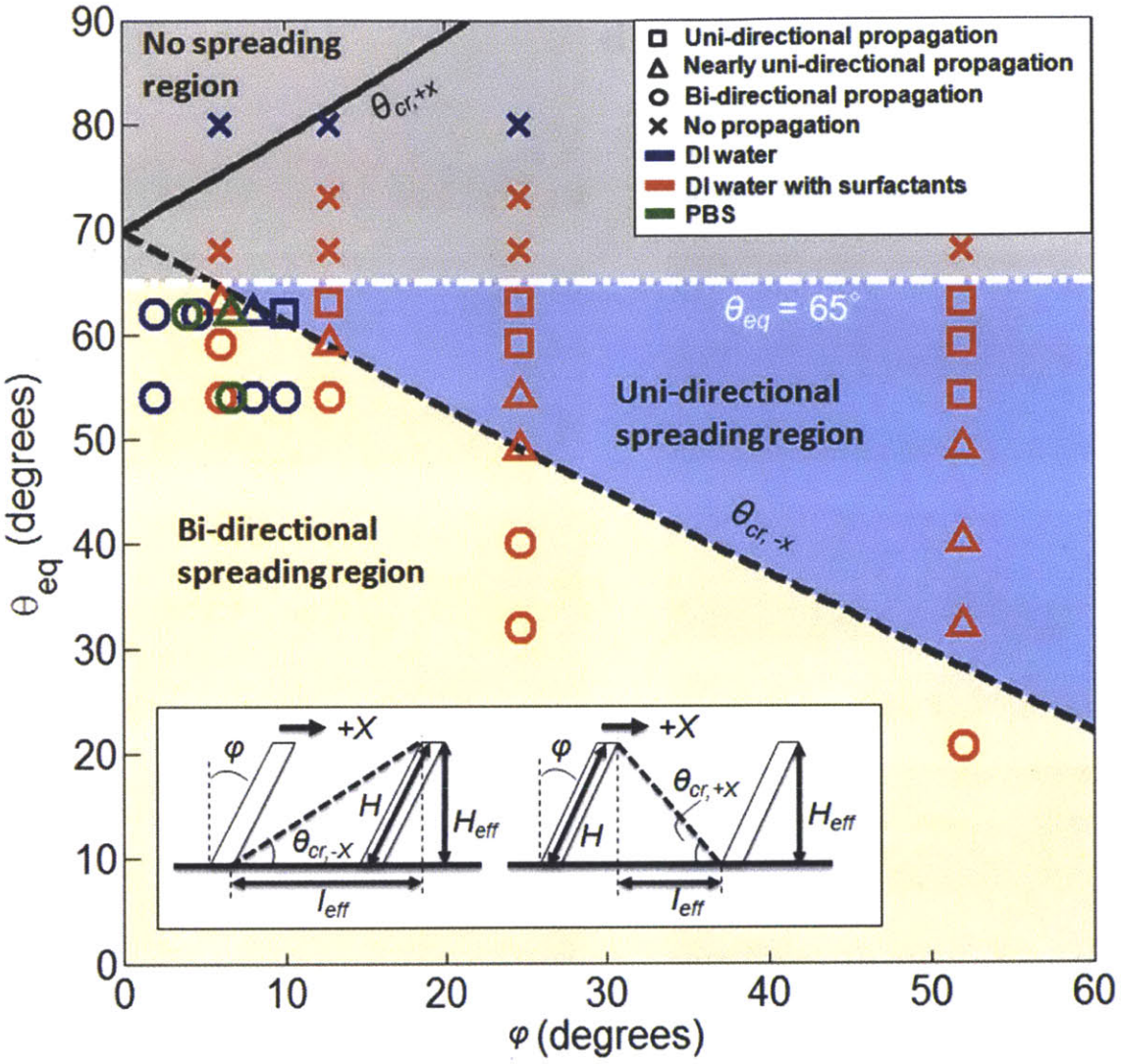

Figure 2-6. Experimental results and the theoretical curves predicting uni-directional liquid spreading. The fabricated asymmetric pillars have diameters ranging from 500 nm to 750 nm, spacings of 3.5 μm, and heights of 10 μm. The squares (□), circles (○), triangles (Δ), and crosses (×) show experimental results of uni-directional, bi-directional, nearly uni-directional, and no liquid propagation, respectively. The colors of those symbols indicate the different liquids used in the experiments. The theoretical curves based on the proposed model are shown for $\theta_{eq} = \theta_{cr}$ with varying deflection angles, φ, for $H/l = 2.87$. The black solid and dotted curves correspond to the critical contact angles, $\theta_{cr,+x}$ and $\theta_{cr,-x}$. The white dotted line represents the condition for imbibition where $\theta_{eq} = 65°$, obtained by experiments. The center region (blue) bound by $\theta_{cr,-x}$ and $\theta_{eq} = 65°$ represents the parameter space that leads to uni-directional liquid spreading. Inset: Schematics explaining the geometries for the proposed model to determine the critical angle, θ_{cr}, in the –X (left) and +X (right) directions.

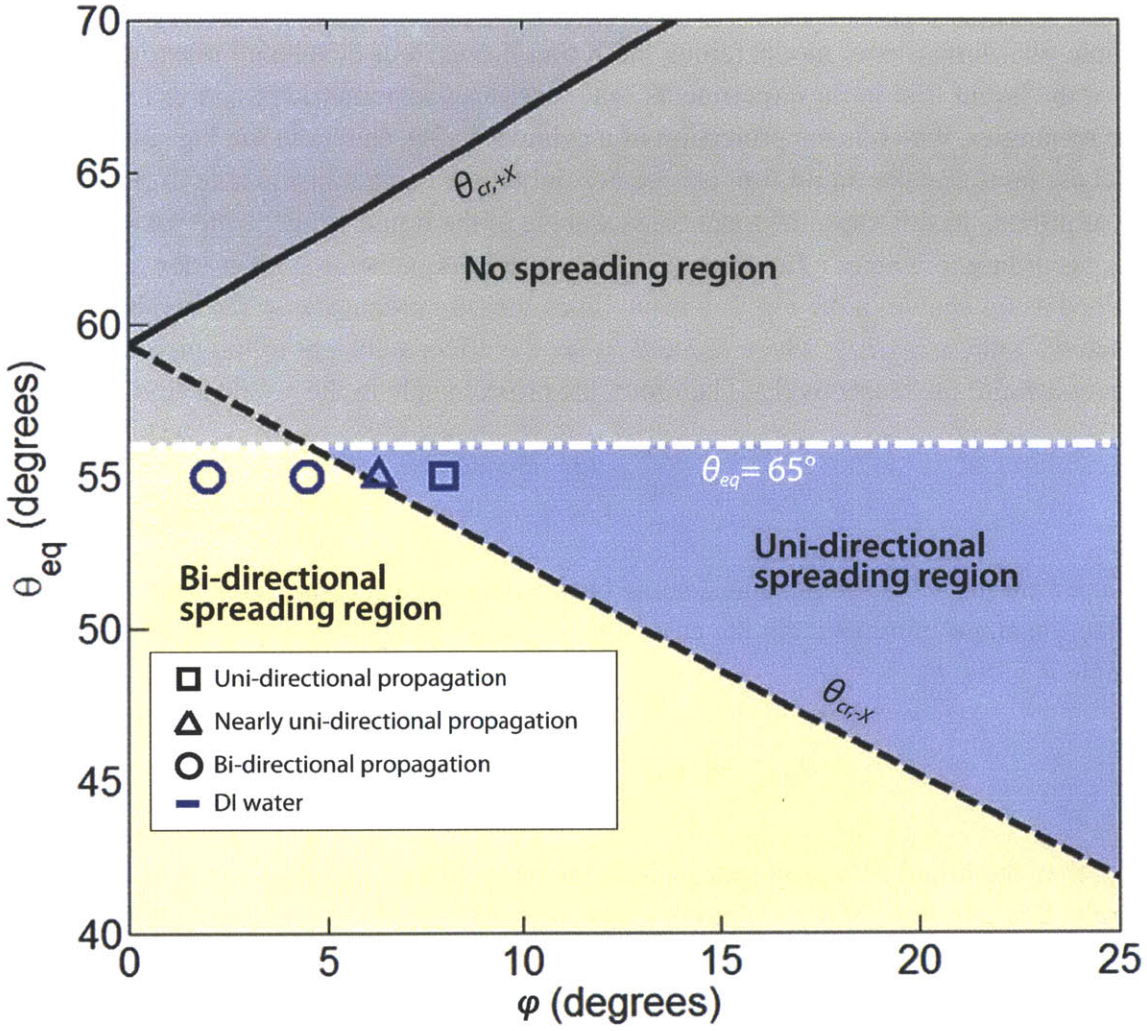

Figure 2-7. Experimental results and the theoretical curves predicting uni-directional liquid spreading for H/l = 1.71. The fabricated asymmetric pillars have diameters ranging from 500 nm to 750 nm, spacings of 3.5 μm, and heights of 6 μm. DI water was tested on nanopillar arrays with deflection angles of 2°, 4.5°, 6.3°, and 7.5° on the polymer, p(NIPAAm-co-DEGDVE), coated surfaces. The intrinsic contact angle with DI water on the surfaces is 54°. The squares (□), circles (○), and triangles (Δ) show experimental results of uni-directional, bi-directional, and nearly uni-directional liquid propagation, respectively. The center region bound by $\theta_{cr,-x}$ and θ_{eq} = 56°, obtained by experiments, represents the parameter space that leads to uni-directional liquid spreading. For this different H/l ratio=1.71, the model and experiments also show excellent agreement.

2.4 Geometrical Model

A simple two-dimensional model (along the X and Z axes) was developed to explain the behavior of the liquid film in the experiments. The fabricated asymmetric pillars were simplified as slanted rectangles, which is the projection of a cylinder in 2D, shown in the Fig. 2-6 inset. The model assumes that the liquid film propagates only if the contact line is able to reach the next row of pillars. In this case, the local contact angle of the liquid which is the intrinsic contact angle, θ_{eq}, according to Young's Equation [72, 79] must be equal to or smaller than a critical angle defined as θ_{cr} shown in the Fig. 2-6 inset. Since the film propagates at the height of the pillars, then $\theta_{cr} = \tan^{-1}(H_{eff}/l_{eff})$, where H_{eff} and l_{eff} are the effective height of the pillars and spacing between pillars, respectively. Therefore, the critical angle in the +X direction is given by

$$\theta_{cr,+x} = \tan^{-1}\frac{(H/l)\cos\varphi}{1-(H/l)\sin\varphi} \quad (1)$$

where H and l are the actual height and spacing between the pillars, respectively, and φ is the pillar deflection angle. Similarly, for the case of liquid film propagation in the –X direction, the critical angle is given by

$$\theta_{cr,-x} = \tan^{-1}\frac{(H/l)\cos\varphi}{1+(H/l)\sin\varphi}. \quad (2)$$

If $\theta_{cr} > \theta_{eq}$, then the liquid film propagates within the nanopillars, otherwise, the liquid film pins. Equivalently, this criterion for liquid film propagation can be obtained because θ_{eq} is the lowest energy state from Young's Equation and the contact angle of the liquid cannot be smaller than θ_{eq} during the propagation process.

The model is overlayed with the experimental results for the case $\theta_{cr} = \theta_{eq}$ in Fig. 2-6 on asymmetric nanopillars where the H/l ratio is 2.87 (see Fig. 2-7 for the results in the case of a H/l ratio of 1.71). The curves, $\theta_{cr,+x}$ and $\theta_{cr,-x}$, separate the domains of control parameters, θ_{eq} and φ, where the liquid film propagates and pins in the +X and –X directions based on the model. In addition, the condition for imbibition needs to be satisfied for the liquid to spread on the surface[11]. Using theory, the imbibition contact angle for pillar diameters of 500 to 750 nm ranges from 60° to 66.5°. However, due to the roughness on the sides and the variations in diameters of the fabricated pillars, we found through experiments that the imbibition contact angle is approximately 65° for all of the surfaces. As a result, the region in the center bound by $\theta_{cr,-x}$ and $\theta_{eq} = 65°$ represents the parameter space of θ_{eq} and φ that leads to uni-directional liquid film propagation. Despite the simplifications in the proposed model, the experiments and model show excellent agreement. The spreading phenomenon is in fact three-dimensional and involves complex menisci shapes, but the criterion for spreading is determined by whether the contact line can reach the next row of pillars, which is well captured by the 2-D model. In addition, for these

fabricated geometries, the liquid equilibrates along the Y-axis faster than along the X-axis. Therefore, liquid propagation occurs primarily along the X-axis, and the proposed 2-D model can well-predict uni-directional spreading. Close to the lower boundary of the domains, however, the liquid is nearly pinned, which is most likely due to the defects in the nanostructures created during the fabrication process, and hence, allows the liquid contact line to reach the next row of pillars.

2.5 Conclusion

We demonstrate the manipulation of liquid spreading using asymmetric nanostructured surfaces. Asymmetric nanopillar arrays were fabricated with diameters of 500 to 750 nm and deflection angles of 3 to 52 degrees using deep reactive ion etching and angled metal deposition process on silicon. Droplets can achieve uni-directional, nearly uni-directional, and bi-directional spreading behaviors on asymmetric nanostructured surfaces with different deflection angles. A theory based on an energy argument is also developed to predict the spreading behaviors and shows excellent agreement with experimental results. The work offers insights into the design of asymmetric nanostructures and exciting opportunities to achieve uni-directional liquid spreading. In the future, tunable nanostructures or asymmetric nanostructures with externally applied fields can be used for real-time control of spreading behavior. Most importantly, the work that manipulation liquid spreading with structured surfaces is promising, which potentially can be used to manipulate vapor bubble dynamics.

Chapter 3 Structured Surfaces for Enhanced Pool Boiling Heat Transfer

3.1 Introduction

Thermal management using two-phase cooling has received significant interest for high flux applications including concentrated photovoltaics, GaN power amplifiers, and integrated circuits due to the large latent heat associated with phase change [14, 15, 90, 91]. The critical heat flux (CHF) represents the operational limit in a two-phase (boiling) heat transfer system marking the point when a vapor film will begin to cover the heated surface, significantly reducing heat transfer efficiency. Therefore, methods to extend CHF have been studied extensively owing to its significant practical importance in high performance thermal management systems [26, 92, 93]. In pool boiling, CHF has traditionally been attributed to a surface-independent hydrodynamic mechanism associated with the Helmholtz instability [21]. However, recent investigations have highlighted the important effect of surface wettability on boiling heat transfer by demonstrating significant enhancements in CHF using micro/nanostructured surfaces[60, 61, 63, 94, 95]. For example, Chen *et al.* [60] showed more than 100% enhancement in CHF (~200 W/cm^2) with water as the working fluid by structuring the heat transfer surface with silicon and copper nanowire arrays. Subsequently, Kim *et al.*[94] demonstrated a CHF of ~230 W/cm^2 on a hierarchical surface comprised of a silicon micropillar array covered with ZnO nanowires. While past studies have focused on synthesizing small feature sizes to improve surface wettability [60, 63, 94-96], the precise role of capillary-length-scale surface roughness on CHF is poorly understood, particularly in the complete wetting regime where the apparent liquid contact angle is zero and a range of CHF values have been reported [60, 63, 92, 94, 96]. In this paper, we studied nucleate boiling on horizontally-oriented, well-defined microstructured surfaces to systematically investigate the role of roughness-augmented wettability on CHF. To interpret our experimental results, we used an analytical force balance model to predict CHF in the complete wetting regime which shows good agreement with the experimental data in this work and from the literature. Our study supports the view that roughness augments the capillary force pinning the contact line of bubbles on the surface resulting in CHF enhancement.

3.2 Microstructured Surfaces

To investigate the effect of roughness-augmented wettability on CHF, we microfabricated structured surfaces with roughness factors r, defined as the ratio of the true area in contact with the liquid to the projected area, ranging from 1.79 to 5.94. Figure 3-1 shows scanning electron micrographs (SEMs) of representative microstructures fabricated for this study. The micropillar arrays were etched in undoped silicon using deep reactive ion etching (DRIE). A 300 nm thick thermal oxide layer was subsequently grown to enhance surface wettability and a 500 nm thick copper layer was deposited on the back side of the samples to facilitate attachment by soldering

to the experimental setup. The etched wafers were diced into samples measuring 2 x 2 cm, which is large enough to be considered representative of an infinite plate [95, 97] and of comparable size to high heat flux electronic components. Smooth oxidized samples were also prepared for comparison. The heat transfer performance of the microstructured surfaces was measured using an experimental boiling setup.

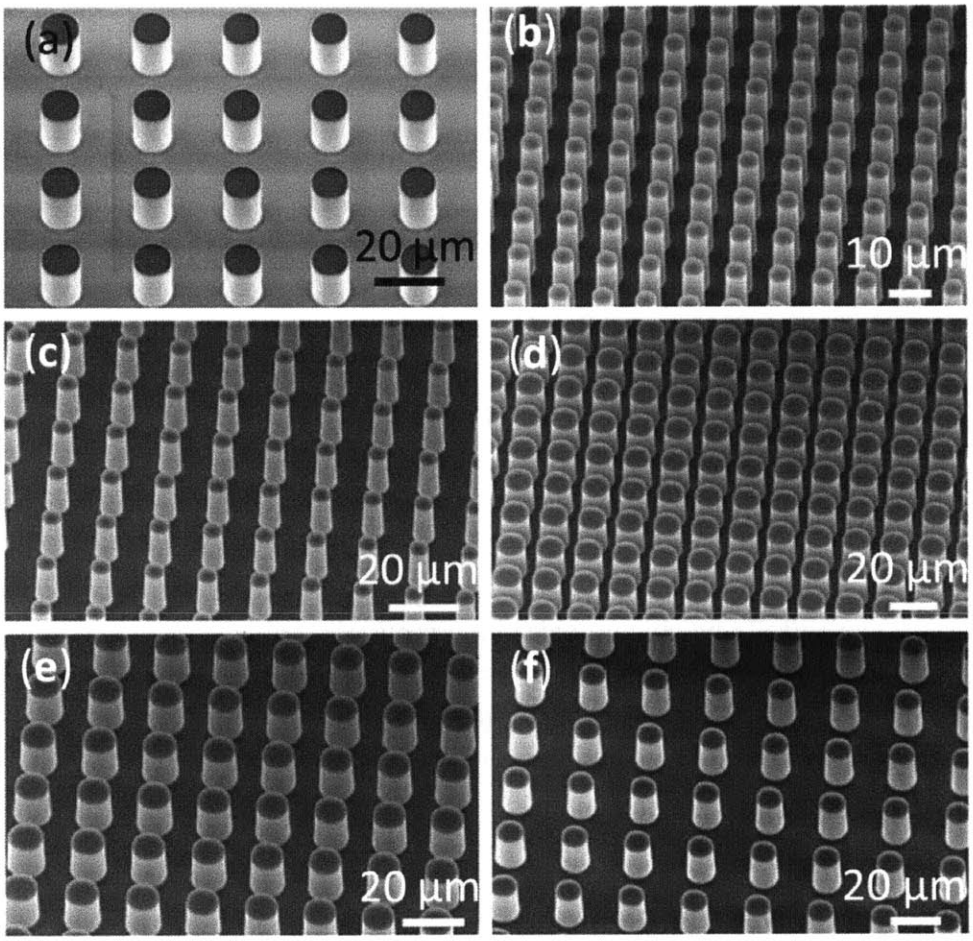

Figure 3-1. Scanning electron micrographs (SEMs) of the fabricated silicon microstructured surfaces. The pillars have heights of (**a**) 10 μm and (**b-f**) 20 μm; center-to-center spacings of (**a, f**) 15 μm, (**b, d**) 5 μm, and (**c, e**) 10 μm; and diameters of (**b, c**) 5 μm and (**a, d-f**) 10 μm.

3.3 Pool Boiling Experiments

The pool boiling setup (Fig. 3-2) consisted of an oxygen-free copper block and a tempered glass chamber fixed at both ends by Ultem mounts. Five cartridge heaters were imbedded in the copper block allowing for a maximum power of 1400 W (350 W/cm^2). The microstructured surfaces were bonded to the copper block using solder paste (Delta 717D, Qualitek) to ensure good attachment with minimal thermal resistance and the surface was maintained in a horizontal orientation for all of the experiments. Five in-line K-type thermocouples (KMQSS-020,

OMEGA) were inserted into the center axis of the copper block with the topmost thermocouple located right beneath the sample. Note that the flux area of the copper block matched the structured sample area. The heat flux was therefore determined based on the linear temperature gradient of the middle three thermocouples using Fourier's law. The surface temperature was determined from the temperature measured by the topmost thermocouple, the measured heat flux, the measured thickness of the sample (600-670 μm), and the thermal conductivity of silicon, while the lowest thermocouple was used for reference only. A sheathed K-type thermocouple (KQSS-18U-12, OMEGA) was positioned 2 cm above the mounted sample to monitor the pool temperature. In the experiments, temperature was recorded with the thermocouple logger (18200-75, Cole-Parmer). In all of the experiments, the steady state condition was determined based on the criterion that the temperature change measured by the thermocouples in the copper block was less than 0.5 K over 1 minute. This condition was typically satisfied within 5 - 8 minutes of changing the input power, which was done in steps ranging from 50 W to 100 W. Based on this procedure, the difference between the assumed steady state temperature and the asymptotic value using an exponential curve fit to the measured temperatures as a function of time was less than 2%. To minimize losses, the chamber was wrapped in guard heaters and a layer of dense fiber glass insulation allowing the pool to be maintained at saturation temperature during the experiment. During the experiments, the chamber was vented to the atmosphere through a coil reflux condenser (QC-6-4, Quarkglass) at the top of the setup. Chilled water was circulated through the reflux condenser such that the vapor was condensed back to the pool.

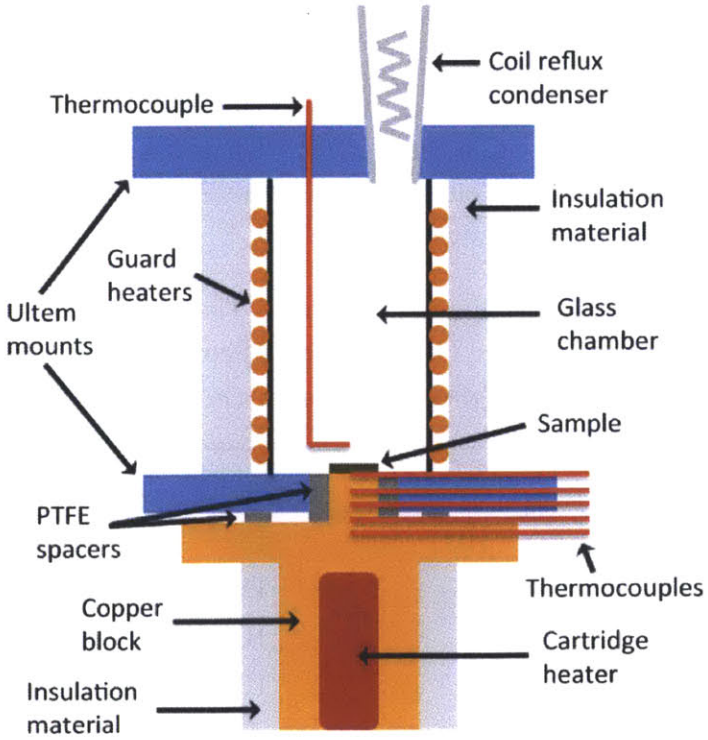

Figure 3-2. Schematic of the experimental pool boiling setup.

The uncertainty of the measurements was estimated based on the variation of thermal conductivity of copper with temperature, the resolution of the thermocouples, the accuracy of the thermocouple logger, and the precision of the thermocouple location. The uncertainty of the absolute temperature measurement of the thermocouple (KMQSS-020, OMEGA) was 1.1 K and the resolution of the thermocouple logger was 0.7 K, such that the overall uncertainty of the temperature measurement was 1.8 K. The variation in the thermal conductivity of copper with temperature was estimated using a linear fit. The uncertainty of thermocouple location was approximately 250 μm. Therefore, the total uncertainty in the heat flux was less than 5.6% as determined by the propagation of errors. For all tests, degassed, high purity water (Chromasolv for HPLC, Sigma-Aldrich) was used to avoid premature bubble formation and minimize surface contamination.

3.4 Experimental Results

The heat flux q'' as a function of wall superheat $\Delta T = T_w - T_{sat}$, where T_w is the heated surface temperature and T_{sat} is the saturation temperature, for the smooth and microstructured SiO_2 surfaces is shown in Fig. 3-3. The maximum uncertainty of the heat flux and temperature measurements was ~5.6% and 1.8 K, respectively. Details of the pillar geometries tested are listed in Table I. Note that in the calculation of the roughness factor, the scalloped features on the sidewall of micropillars were accounted for by multiplying the pillar height by a factor of $\pi/2$ [98]. Compared with the results on the smooth surface (Sm), the boiling curves showed a significant enhancement in CHF on the structured surfaces (S1-S6). A CHF of 207.9 ± 9.9 W/cm^2, which is comparable to the highest CHF value reported in previous studies on nanostructured surfaces [60, 63, 94, 95], was achieved with a $\Delta T = 39.3 \pm 1.8$ K on S6. The results demonstrate the positive correlation between the CHF and surface roughness factor. In addition, the two nearly identical boiling curves for the smooth surface (Sm) demonstrate the consistency and accuracy of the measurements.

TABLE I: Geometric parameters of the micropillar arrays. The units of height, diameter and (center-to-center) spacing are in microns. The roughness of contact line, r, and solid fraction, φ, are calculated by: $r = 1 + \pi d\, h(\pi/2)/(d+s)^2$ and $\varphi = (\pi d^2/4)/(d+s)^2$, respectively.

Sample No.	Height (h)	Diameter (d)	Spacing(s)	r	φ
S1	10	10	15	1.79	0.13
S2	20	10	15	2.58	0.13
S3	20	5	10	3.19	0.09
S4	20	10	10	3.47	0.20
S5	20	10	5	5.39	0.35
S6	20	5	5	5.94	0.20

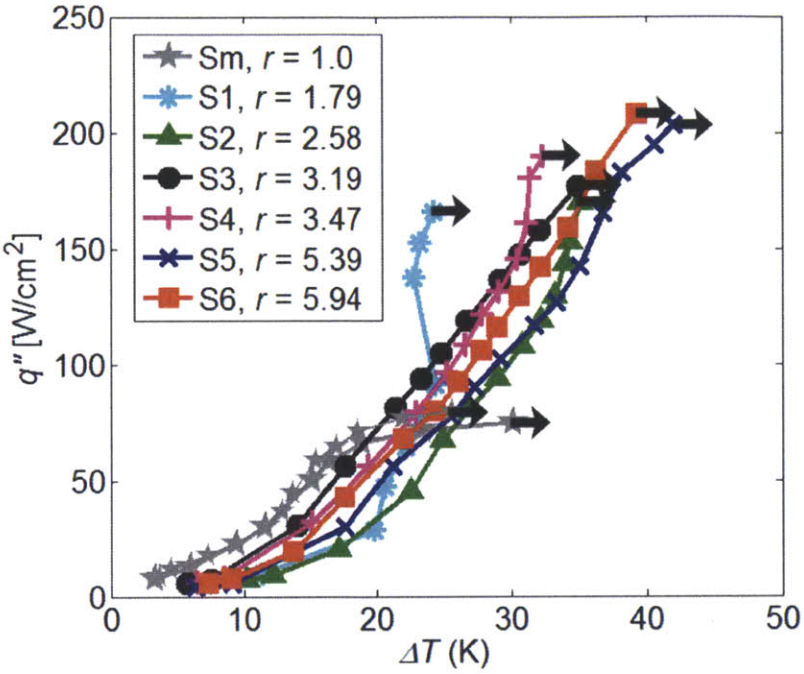

Figure 3-3. Boiling curves on the smooth ($r = 1$) and microstructured ($r > 1$) surfaces detailed in Table I. The arrows indicate the CHF condition. The consistency and accuracy of the measurements are demonstrated by the two nearly identical boiling curves for the smooth surface. The boiling curves show a clear trend of increasing CHF with surface roughness factors due to roughness-augmented capillary forces.

3.5 CHF Model

To understand and predict CHF on structured surfaces where the liquid wets the surface completely, a model incorporating surface properties (*i.e.*, surface roughness factor r) is required. While a detailed understanding of the CHF mechanism is still lacking [99], it is clear that surface wettability is a key factor dictating CHF [27, 30, 97, 99-102]. Recent works have used the capillary pumping mechanism, which assumes that there is insufficient liquid supply to balance the rate of evaporation, to predict CHF on structured surfaces [30, 60]. However, this model over-predicted CHF values on our microstructured surfaces (17-120× greater than the experimental results), which suggests another mechanism dominates CHF in this case. Kandlikar presented a simplified force-based analysis for smooth surfaces assuming that there is sufficient liquid supply at CHF. Momentum, buoyancy, and surface forces at the liquid/vapor interface of an individual bubble were considered [26]. If the combination of surface and buoyancy forces compensate the momentum force during the growth phase of the bubble, the hot/dry area developed at the base of bubble during growth can rewet upon departure. Otherwise, the hot/dry area will expand irreversibly leading to the CHF condition [99, 102]. However, in recent studies the data comparing the predictions of the Kandlikar model to the CHF

behavior on structured surfaces was typically presented as a function of apparent contact angle β, which leads to crowding when $\beta \rightarrow 0$ [63, 94]. This result is attributed to the fact that the model couples bubble geometry and the surface force through the macroscopic contact angle [26]. Thus, on superhydrophilic surfaces the model cannot account for a wide variety of structured surfaces that display no apparent contact angle, *i.e.*, $\beta = 0$ [60, 63, 94]. To address this issue, we modified the force-balance-based model to predict CHF on superhydrophilic surfaces ($\beta = 0$). In this regime, the microlayer (which includes the structures) underneath the bubble dries out such that a "Wenzel" bubble [4] is formed at CHF [99]. Figure 3-4 shows the horizontal components (x-axis) of forces acting on the "Wenzel" bubble [4], where a vapor film appears underneath the bubble on structured surfaces. At low heat fluxes, the vapor bubble would depart at a certain size if the surface forces and buoyancy force can overcome the force due to the momentum change, which allows the liquid to wick inside the structures. At high heat fluxes, however, the surface forces and the buoyancy force can no longer maintain the balance against the momentum force due to rapid evaporation and, as a result, the vapor expands horizontally covering the whole surface leading to the CHF condition.

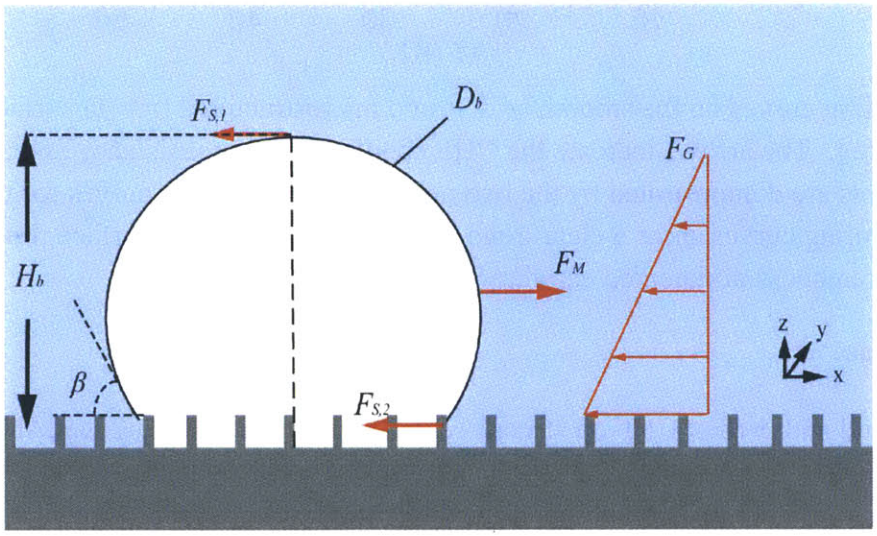

Figure 3-4: Schematic diagram of forces acting on the vapor bubble on a structured surface adapted from Kandlikar [26]. At CHF, the vapor film forms within microstructures beneath the bubble, *i.e.*, "Wenzel" bubble. Here F_M represents the force due to momentum change while F_G represents the buoyancy force, and $F_{S,1}$ and $F_{S,2}$ are surface forces. β is the apparent liquid receding angle on the structured surface, H_b is the height of the bubble and D_b is the diameter of the bubble.

When we consider half of the bubble and the forces acting on it in the direction parallel to the surface, for a unit length in the direction normal to the plane of Fig. 3-4 (y-axis), the surface force $F_{S,1}$ is given by

$$F_{S,1} = \sigma_{lv}, \tag{1}$$

where σ_{lv} is surface tension. On structured surfaces, the surface force, $F_{S,2}$, at the bottom of the bubble is amplified due to a longer effective contact line length, which is the unit length multiplied by the surface roughness factor, r

$$F_{S,2} = \sigma_{lv} \times r \cos\theta_{rec}, \tag{2}$$

where r is surface roughness, and θ_{rec} is intrinsic receding contact angle of liquid.

The momentum force is the result of evaporation at the interface. Here, the interface is characterized as a plane with bubble height, H_b and a unit width normal to plane (y-axis) and the evaporation rate is considered to be uniformly distributed across the interface. The force due to momentum change, F_M, is given by the product of the evaporation mass flow rate and the vapor velocity relative to the interface,

$$F_M = \frac{q_l'' H_b 1}{h_{fg}} \times \frac{q_l''}{h_{fg}} \frac{1}{\rho_g} = \left(\frac{q_l''}{h_{fg}}\right)^2 \frac{1}{\rho_g} H_b, \tag{3}$$

where q_l'' is the heat flux due to evaporation per unit area at interface, h_{fg} is the latent heat, and ρ_g is the vapor density. The bubble height is related to the bubble departure diameter D_b as

$$H_b = \frac{D_b}{2}(1 + \cos\beta), \tag{4}$$

where β is apparent liquid receding angle as shown in Fig. 3-4. The heat flux on the surface can be obtained by approximating the interface as a half cylinder with diameter D_{ave} and height H_{ave}. Here D_{ave} corresponds to the average diameter as the bubble grows and is taken as $D_{ave} = D_b/2$ as a first approximation such that $H_{ave} = (D_{ave}/2)(1 + \cos\beta)$. In addition, during the bubble growth, heat is removed from the surface within the influence area, which is considered as a circle with diameter of L. Therefore, the heat flux on the surface is given by

$$q'' = \frac{q_l''(D_{ave}/2)(1 + \cos\beta)\,(\pi D_{ave})/2}{(\pi/4)L^2} = (1 + \cos\beta)\left(\frac{D_b}{2L}\right)^2 q_l'' \tag{5}$$

The buoyancy force, F_G, in the direction parallel to the surface (z-axis), as a result of the distributed hydraulic pressure shown in Fig. 3-4, is obtained by

$$F_G = \frac{1}{2} g(\rho_l - \rho_g) H_b \times H_b \times 1 \times \cos\psi, \tag{6}$$

where ψ is the inclined angle of heated surface and ρ_l is the liquid density. CHF occurs when F_M is greater than the sum of $F_{S,1}$, $F_{S,2}$, and F_G. Therefore, at CHF, the force balance yields

$$F_M = F_{S,1} + F_{S,2} + F_G. \tag{7}$$

Substituting Eqs. (1), (2), (3), (4) and (6) into (7), replacing q_l'' with q'' using Eq. (5) and assuming $r\cos\theta_{rec} = \alpha$, the heat flux at CHF, $q'' = q_c''$, is obtained as

$$q_c'' = h_{fg}\rho_g^{1/2}\left[\frac{(1+\cos\beta)}{4}\right]\left[\sigma_{lv}\frac{2(1+\alpha)}{(1+\cos\beta)}\frac{{D_b}^3}{L^4} + g(\rho_l-\rho_g)\frac{{D_b}^5}{4L^4}(1+\cos\beta)\cos\psi\right]^{1/2}. \tag{8}$$

We can scale the diameters D_b and L by the capillary length, λ_c,

$$\lambda_c = \left[\frac{\sigma_{lv}}{g(\rho_l-\rho_g)}\right]^{1/2}, \tag{9}$$

which gives

$$D_b = C_1\lambda_c, \tag{10}$$

$$L = C_2\lambda_c. \tag{11}$$

Then, the heat flux in Eq. 8 becomes

$$q_c'' = h_{fg}\rho_g^{\frac{1}{2}}\left[\frac{(1+\cos\beta)}{4}\right]\left[\frac{{C_1}^3}{{C_2}^4}\frac{2(1+\alpha)}{(1+\cos\beta)} + \frac{{C_1}^5}{{C_2}^4}\frac{1}{4}(1+\cos\beta)\cos\psi\right]^{1/2} \times\left[\sigma_{lv}g(\rho_l-\rho_g)\right]^{1/4}. \tag{12}$$

Following the set of assumptions made by Kandikar [26], where D_b is half the wavelength of the Taylor instability ($C_1 = \pi$) and L is $2D_b$ ($C_2 = 2\pi$), Eq. 12 becomes

$$q_c'' = K \times h_{fg}\rho_g^{1/2}[\sigma_{lv}g(\rho_l-\rho_g)]^{1/4}, \tag{13}$$

with

$$K = \left(\frac{1+\cos\beta}{16}\right)\left[\frac{2}{\pi}\frac{(1+\alpha)}{(1+\cos\beta)} + \frac{\pi}{4}(1+\cos\beta)\cos\psi\right]^{1/2}.$$

Recent studies have verified that at CHF in pool boiling bubble departure diameters are less than 1 mm [99, 103]. However, the wavelength of the Taylor instability is ~16 mm for water at a saturation temperature of 100 °C, which leads to D_b of ~8 mm based on the half wavelength assumption. In addition, the assumption that the diameter of the influence area L is $2D_b$ is based on work studying the area where superheated liquid is carried away by a departed bubble [104]. It is not clear whether the surface area where heat enters into a vapor bubble during phase change

can be seen as the area affected when the bubble departs. Despite the utilization of these estimated parameters, the agreement between experimental data and the model proposed suggests a plausible framework to explain the effect of roughness-augmented capillary forces on CHF. However, the most important argument for this new model (Eq. 13) is that the surface force per unit length maintaining the position of the contact line is amplified due to a longer effective contact line length, which can be estimated, assuming a bubble size larger than the underlying roughness length scale, as the unit length multiplied by the surface roughness factor. Also note that when $\alpha < 1$, Eq. 13 simplifies to Kandlikar's model. In this form, the surface force is no longer coupled with the bubble geometry such that Eq. 13 is well-defined in the complete wetting regime where $\cos\beta = 1$, but $\alpha > 1$.

To demonstrate the applicability of Eq. 13, the predicted CHF as a function of α was overlaid with data from our experiments and previous studies [60, 63, 94] in Fig. 3-5. Also plotted for comparison is the CHF predicted by the classical Kutateladze-Zuber (K-Z) model [21, 22] (hydrodynamic instability mechanism) using an empirical factor of $K = 0.18$ in Eq. 2 [105]. The r values for Chen *et al.*[60], Kim *et al.*[94] and Ahn *et al.*[63] were estimated based on the reported geometrical parameters and SEMs. These values may be inaccurate due to the fact that the surface roughness factor was, either, not explicitly reported or the calculation method was not detailed. In addition, contact angles reported in the literature are typically equilibrium values (θ_{eq}) measured at room temperature [60, 63, 94, 95]. Since the surface wettability is a key parameter in determining CHF, the dependence of contact angle and surface tension on temperature should be accounted for [26, 27, 99]. Therefore, to compare the data with our CHF model, estimations for contact angles at the saturation temperature, $T_{sat} = 100$ °C, were made. The dependence of contact angle and surface tension on temperature has not been consistently addressed in the context of pool boiling [26]. In order to better characterize the roughness-augmented wettability, we estimated the contact angle at the saturation temperature. Here, we estimated the variation of $\cos\theta$ with temperature from the Young-Dupré equation [106],

$$\cos\theta\,(T) = W_{ls}/\sigma_{lv}\,(T) - 1, \tag{14}$$

where $\sigma_{lv}(T)$ is the temperature-dependant liquid-vapor surface tension [107] and W_{ls}, the work of adhesion between the liquid and solid, was estimated as

$$W_{ls} \approx 2\sqrt{\sigma_{sv}^{d}\sigma_{lv}^{d}(T)} \tag{15}$$

where σ_{sv} is the solid-vapor surface tension and the superscript, d, represents the dispersive component of surface tension. This form implies that dispersive forces dominate the wetting behavior and neglects both polar and hydrogen-bonding interactions between the liquid and solid. For non-polar interactions, such as in water/hydrocarbon systems, Eq. 15 has been shown to be quite accurate [106]. In the case of water/oxide interfaces, this approximation is not strictly true due to the presence of OH groups on the surface. However, under typical experimental

conditions, contamination is always present on the surface due to the adsorption of atmospheric hydrocarbon species to the OH groups [108]. Therefore we make the simplifying assumption that the hydroxides are shielded from the water molecules. The dispersive component of the surface energy of water has been estimated as $\sigma_{lv}^{d} = 20 \pm 2$ mJ/m^2 at $T = 293$ K [109]. However, the refractive index of water demonstrates a non-negligible variation with temperature. Accordingly, the dispersive component of water was determined from the following approximation

$$\sigma_{lv}^{d}(T) = \frac{A(T)}{24\pi D_0} \tag{16}$$

where D_o (= 0.165 nm) is a representative cut-off distance for the interaction [106]. The Hamaker constant A can be estimated from Lifshitz theory for nonretarded van der Waals interactions as

$$A(T) = \frac{3}{4}kT\left(\frac{\varepsilon(T)-1}{\varepsilon(T)+1}\right)^2 + \frac{3h\nu}{16\sqrt{2}}\frac{(n(T)^2-1)^2}{(n(T)^2-1)^{3/2}} \tag{17}$$

where k and h are Boltzmann and Planck constant, respectively, ν (~3×10^{15} 1/s) is the primary electronic adsorption frequency, $\varepsilon(T)$ is the temperature-dependent dielectric constant [107], and $n(T)$ is the temperature-dependent refractive index [110]. At T_a (= 293 K), Eq. 16 predicts $\sigma_{lv}^{d} = 18.2$ mJ/m^2, which compares well with the value determined from detailed calculations[108]. Furthermore, σ_{sv}^{d} should be only a weak function of temperature, varying by less than 1% over the investigated range from ambient to saturated boiling conditions as indicated by a calculation of the Hamaker constant [106]. The solid/vapor dispersive component σ_{sv}^{d} is then estimated by fitting Eq. 14 using the measured value of θ at ambient conditions. In neglecting non-dispersive interactions between the solid and liquid, we expect that our fitting procedure may over-predict the magnitude of the $\cos\theta$ increase with increasing temperature.

For our thermally-grown SiO_2 sample, goniometer measurements on a smooth surfaces demonstrated a value of θ_{rec} =25.4° ± 2.3° at T_a, where θ_{rec} is the liquid receding angle. This value of the contact angle is indicative of adsorbed hydrocarbon species, since a clean SiO_2 surface will be completely wetted by water [108, 111]. After performing the boiling experiment, the contact angle was found to vary between the value measured before experiment and θ_{rec} = 32.3° ± 0.4°. This degradation in wettability was attributed to possible organic acid adsorption during the soldering process. As such, this post-boiling value of θ_{rec} was assumed to be indicative of the surface conditions at CHF and was used to extrapolate the surface conditions during boiling. For the extreme value of contact angle, fitting to Eq. 14 suggests σ_{sv}^{d} = 129.6 mJ/m^2, resulting in the estimated $\theta_{rec}(T)$ behavior shown in Fig. 3-6.The calculations predict a decreasing contact angle with increasing temperature until reaching complete wetting at $T \approx 330$ K. A similar fitting procedure was used for the other measured

values of the contact angle, as well as for the nominal room temperature contact angle values reported in the literature for comparison to the predictions of Eq. 13 at T_{sat} = 373 K.

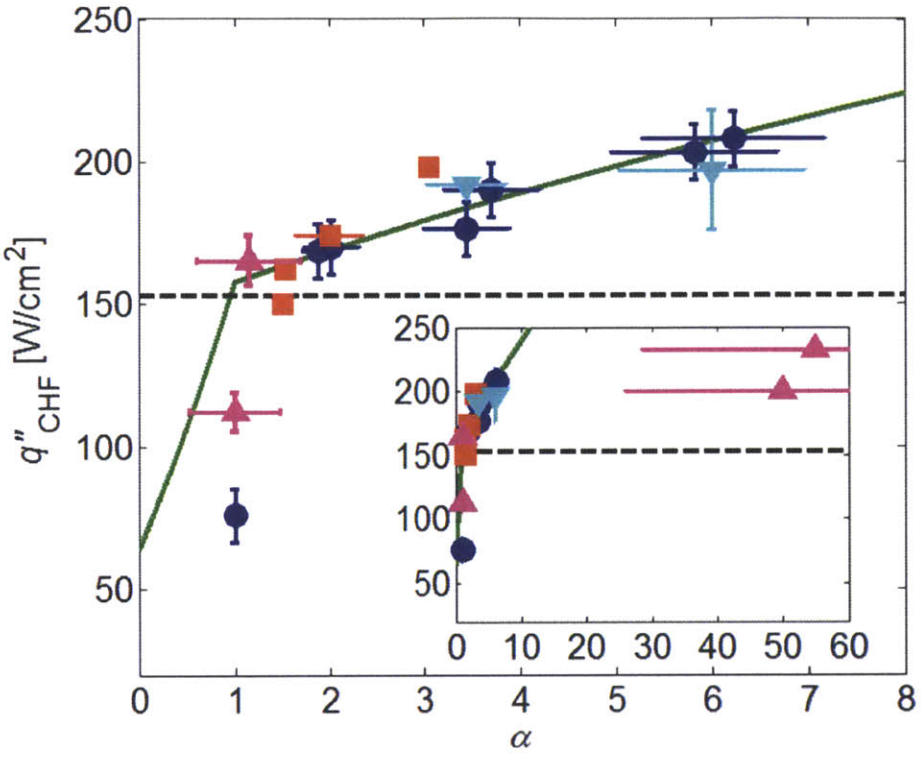

Figure 3-5. CHF as function of α ($= r\,cos\,\theta_{rec}$). The proposed model (solid line) is compared to the K-Z model with a factor of K = 0.18 (dashed line). The symbols show the CHF data from (●) our experiments, (▼) Chen *et al.* [60], (▲) Kim *et al.* [94], and (■) Ahn *et al.* [63], as a function of the estimated α values. The inset shows data from Kim *et al.* with an estimated α ~55.

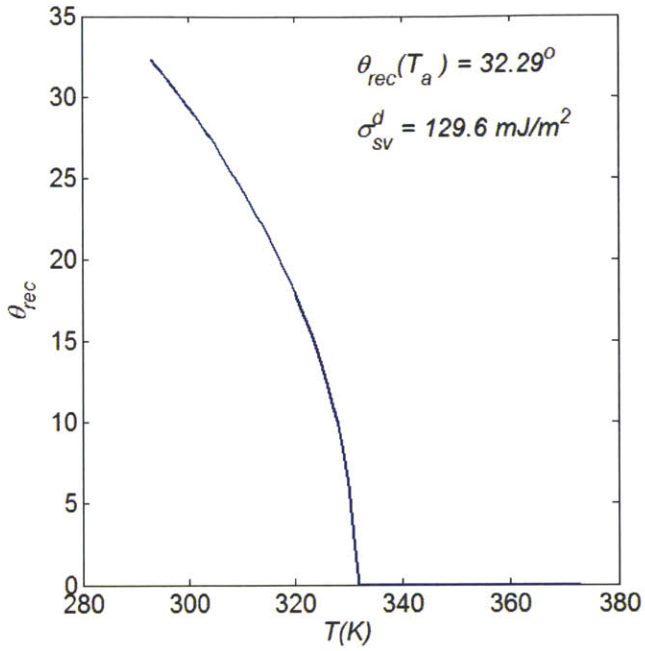

Figure 3-6: Variation in the receding contact angle as a function of temperature estimated from Eq. 14 assuming temperature-independent dispersive solid/vapor interactions. The temperature coefficient is approximately -0.55 °/K.

In Fig. 3-5, the symbols represent the literature data based on our estimates of contact angle at the saturation temperature, while the data based on reported contact angle values are shown in the Supplementary Materials. The difference in α between data from the literature and our estimates [112] demonstrates the potential significance of temperature-dependant liquid contact angle on the amplified surface force (Eq. 2). The error bars for our data along the α-axis are based on the uncertainty in the contact angle measurement at room temperature, while the error bars on α for the literature data are due to fact that only θ_{eq} is reported rather than θ_{rec} [60, 63, 94]. For these cases, α was estimated using $\theta_{eq}/2$ (*i.e.*, average between θ_{eq} and 0) where the error in θ_{rec} ranged from θ_{eq} to 0. The error bars for CHF from Ahn *et al.*[63] were not reported, and are therefore not shown in Fig. 3-5. Note that the estimated α values for the data of Kim *et al.*[94] in the complete wetting regime are shown in the inset of Fig. 3-5 because of the very large estimated α values ($\alpha \approx 55$) due to the large reported surface roughness factor for their nanostructures ($r \approx 50$) and the approximate nature of our temperature-dependent contact angle analysis.

While the value of α has been approximated and simplifications in the extended model exist, the good agreement between the data and model, which does not contain any fitting parameters, suggests that the key physics of the CHF mechanism on these structured surfaces are accounted for. Most importantly, the trend of a small increase in CHF with increasing surface roughness factor, relative to the regime where $\alpha < 1$, is well-captured by the extended model. In addition,

the sudden slope reduction predicted by the extended model at $\alpha = 1$ can explain how the K-Z model remains well-correlated to CHF behavior on a range of typical engineering surfaces studied in the past where $\alpha < 1.5$ (*i.e.*, native metal oxide). The reduction in slope of our model for $\alpha > 1$ suggests that a large increase in surface roughness factor is required to further enhance CHF, which offers significant fabrication challenges. One potential solution, as demonstrated by Kim *et al.*[94], is the use of hierarchical structures comprised of multiple roughness length scales. Following the logic suggested by Eq. 2, the effective roughness of a hierarchical surface is estimated as the product of the roughness factors of each length scale (*i.e.*, $r_{eff} = \prod_1^N r_N$, where r_N is the roughness of each distinct length scale).

3.6 Conclusion

In conclusion, the effect of roughness-augmented wettability on CHF was investigated systemically with well-defined microstructured surfaces. An enhancement in CHF of ~160% was demonstrated on the roughest surface tested. A simple force-balance-based model for CHF in the complete wetting regime was developed to explain the experimentally obtained values. The excellent agreement between the extended model and experimental observation indicates that the roughness-amplified surface force plays the defining role in CHF enhancement on structured surfaces. The issues of contact angle variation with temperature were also addressed and should be considered in future studies given the nature of the CHF mechanism presented here. This study shows new insight of the role of structured surfaces in enhancing CHF and provides basic design guidelines for new surface technologies with high heat removal capability for advanced thermal management applications.

Chapter 4 Hierarchical Surfaces for Critical Heat Flux Enhancement

4.1 Introduction

The large latent heat associated with the liquid-vapor phase transition makes two-phase cooling an ideal approach to address challenges in high heat flux thermal management applications [14, 15, 90, 91]. In a two-phase (boiling) heat transfer system, the critical heat flux (CHF), where a vapor film will begin to cover the heated surface leading to a loss of contact between the surface and liquid, represents the operational limit due to the significant reduction in heat transfer efficiency. Therefore, methods to extend CHF have been studied extensively owing to its significant practical importance in high performance thermal management systems [26, 92, 93]. In chapter 3, we utilized well-defined silicon micropillar arrays to demonstrate the role of increasing surface roughness factor (*i.e.*, r = total surface area/projected surface area) for CHF enhancement on complete wetting surfaces, where the apparent contact angle is $\beta = 0$ [113]. The developed CHF model, based on roughness-amplified capillary forces pinning the contact line of vapor bubbles, showed good agreement with the experimental data for microstructured surfaces with $1 \leq r \leq 6$, with further CHF enhancement predicted for higher values of r [113]. In this work, we fabricated both silica and copper oxide (CuO)-based hierarchical surfaces with $r = 3.6 - 13.3$ to further increase CHF and validate the concept that introducing hierarchy produces a multiplicative effect on contact line pinning forces. Accordingly, we demonstrated $q_c'' \approx 250$ W/cm^2 on the roughest sample tested, representing a ~200% increase in CHF compared to smooth SiO_2 reference surfaces. The obtained CHF values on the hierarchical surfaces were in good agreement with the model prediction, which supports our physical view of the enhancement phenomenon and the multiplicative effect of roughness at distinct length scales. This predictable high heat removal capability using scalable fabrication techniques promises an exciting opportunity for new surface designs for high flux thermal management.

4.2 Surface Roughness Factor and CHF

In chapter 3, the CHF condition was predicted based on a force balance between evaporating vapor momentum, buoyancy, and surface forces acting on the liquid/vapor interface of an individual bubble, leading to an expression in the following form [113]:

$$q_c'' = K \times h_{fg}\rho_g^{1/2}[\sigma_{lv}g(\rho_l - \rho_g)]^{1/4}, \tag{1}$$

where

$$K = \left(\frac{1+\cos\beta}{16}\right)\left[\frac{2(1+\alpha)}{\pi(1+\cos\beta)} + \frac{\pi}{4}(1+\cos\beta)\cos\psi\right]^{1/2},$$

$\alpha = r\cos\theta_{rec}$ is the amplified surface force term, θ_{rec} is the liquid receding angle on the

corresponding smooth surface, σ_{lv} is the liquid-vapor surface tension, and ψ is the inclination angle of the surface (*i.e.*, $\psi = 0$ for a horizontal upward facing surface). In the superhydrophilic wetting regime ($\beta = 0°$), Equation 1 predicts a proportional increase in CHF with the parameter K, which, in turn, is proportional to the square root of the roughness factor r through α, *i.e.*, $q_c'' \propto \sqrt{r}$. Therefore, further enhancement in CHF should increase monotonically with increasing roughness factor. Indeed, we have found that experimental pool boiling data on microstructured surfaces with roughness factors r ranging from 1.8 to 6 follows this scaling, showing reasonable quantitative agreement despite several simplifying assumptions made [113].

4.3 Hierarchical Surfaces

To achieve high roughness factors, we used two fabrication methods to realize hierarchical surfaces with two distinct length scales. Silica-based, superhydrophilic, hierarchical surfaces were fabricated following: (1) A 200 nm thick silicon dioxide (SiO_2) thin film was grown on a silicon wafer. The features were then defined *via* contact lithography with a thin photoresist (OCG-825, Fujifilm), and transferred onto the SiO_2 layer by plasma reactive ion etching (RIE). An oxygen plasma was used to remove residual photoresist and the remaining oxide layer was used as an etch protector. (2) The pillars were etched in silicon using deep reactive ion etching (DRIE). The sample was subsequently placed in a buffered oxide etch (BOE) solution bath to remove remaining SiO_2 layer. (3) A hybrid method consisting of electrostatic self-assembly [114] and electrophoretic deposition (EPD) [115] was employed for coating polymers (polysodium 4-styrenesulfonate, PSS; and Polydiallyldimethylammonium chloride, PDDA) [114] and hydrophilic nanoparticles [115], respectively. EPD is conducted in a 1.0 g/l silicon dioxide nanoparticle suspension, in DI water at pH 8.5. Applied electric potentials were 30 V for 10 sec and 30 sec. (4) Si microstructured coated with SiO_2 nanoparticles is heat-treated at 350 °C for 1 min on a hot plate yields mechanically and thermally robust surfaces. Melting temperatures of PSS and PDDA are slightly higher than 400 °C so the polymers strongly bind the nanoparticles after heat-treatment.

The copper oxide (CuO)-based hierarchical surfaces were fabricated following [116]: (1) A seed layer of Ti/Cu/Ti was first deposited on a silicon (Si) substrate using E-beam evaporation process. The bottom Ti layer (30 nm) was used as an adhesion layer while the Cu layer (350 nm) served as the main seed layer and Ti layer (30 nm) protected the Cu layer from oxidation during the subsequent steps. (2) A thick (80 μm) negative photoresist (KMPR, MICROCHEM) layer was spin coated onto the substrate and patterned using contact lithography to form photoresist-based molds for the electroplating. To ensure the electrolytes wet evenly in the photoresist molds (holes), the molds were subjected to oxygen plasma for 2-10 min to enhance to wettability. (3) The top layer of Ti was first removed with a diluted (1%) hydrofluoric acid (HF) solution. The sample was dipped in a 2M hydrochloric acid (HCl) solution to strip the native oxide layer on the Cu seed layer and then sonicated in the plating bath (Cu 6320, Technic Inc.) for ~30s to facilitate wetting of the molds. During the plating process, we used very low current density (<7 mA/cm^2)

to avoid void formation due to nonuniform current density distribution. After the plating, the photoresist molds were stripped away by the photoresis remover (Remover PG, MICROCHEM). (4) The electroplated Cu micropillar sample was immersed in an alkali solution ($NaClO_2$, NaOH, $Na_3PO_4 \cdot 12H_2O$, and deionized (DI) water) for 5 min to from the sharp needle-like CuO nanostructures on the whole surfaces.

The two fabrication processes are shown schematically in Fig. 4-1, while scanning electron micrographs (SEMs) representative of the realized hierarchical surfaces are shown in Fig. 4-2. Finally, on all surfaces, a 1 μm thick layer of Cu was deposited on the back side of the silicon substrates to facilitate solder attachment of the samples to the test setup, as shown in previous chapter (Fig. 3-2). Upon dicing, the samples had a projected surface area of 2 x 2 cm, which is large enough to be considered representative of an infinite plate [95, 97] and is of comparable size to typical high heat flux electronic components. The heat transfer performance of the hierarchical surfaces was measured using an experimental pool boiling setup (Fig. 3-2) [113]. All tests were performed using degassed, high purity water (Chromasolv for HPLC, Sigma-Aldrich) to avoid premature bubble formation and minimize surface contamination.

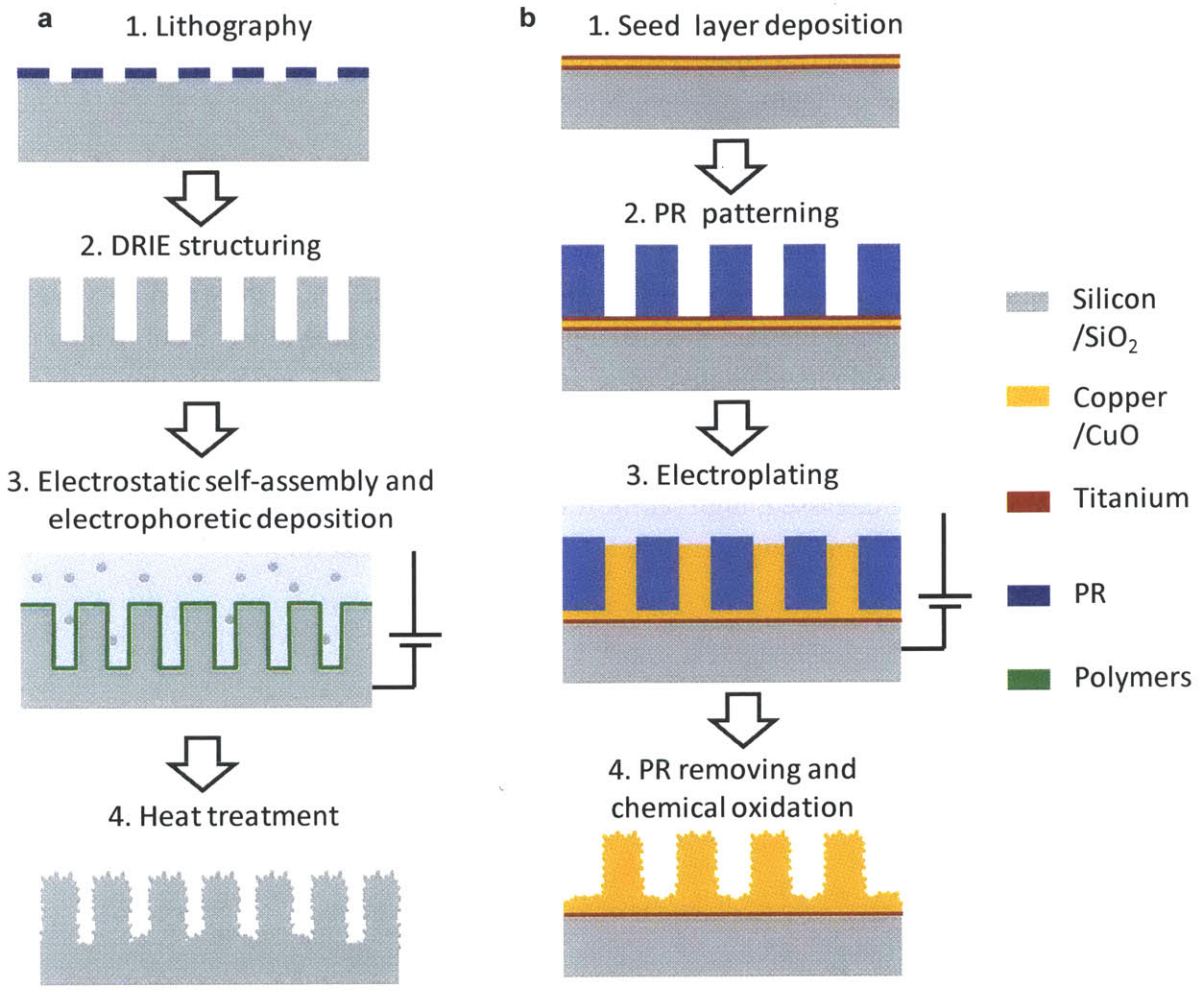

Figure 4-1. Fabrication processes of (**a**) silica and (**b**) CuO-based hierarchical surfaces. EPD-coated silica hierarchical surfaces were fabricated as follows: (1) A photoresist (PR) layer was patterned using photolithography as the etch mask. (2) Si micropillars were made using DRIE. (3) Several layers of polymers (PSS/PDDA) are electrostatically self-assembled on the microstructured surfaces and then 14 nm SiO_2 nanoparticles were deposited with electrophoretic deposition (EPD). (4) The surface is heat-treated at 350 °C to enhace thermal and mechanical durability. CuO hierarchical surfaces were fabricated as follows: (1) Ti/Cu/Ti layers were deposited on a silicon substrate. (2) A thick (~70 μm) PR mold was patterned using photolithography. (3) The top Ti layer was removed to expose the Cu layer and then Cu micropillars were electroplated. (4) After removing the PR, Cu micropillars were oxidized in an alkali solution composed of $NaClO_2$, NaOH, $Na_3PO_4 \cdot 12H_2O$ to form CuO nanostructures.

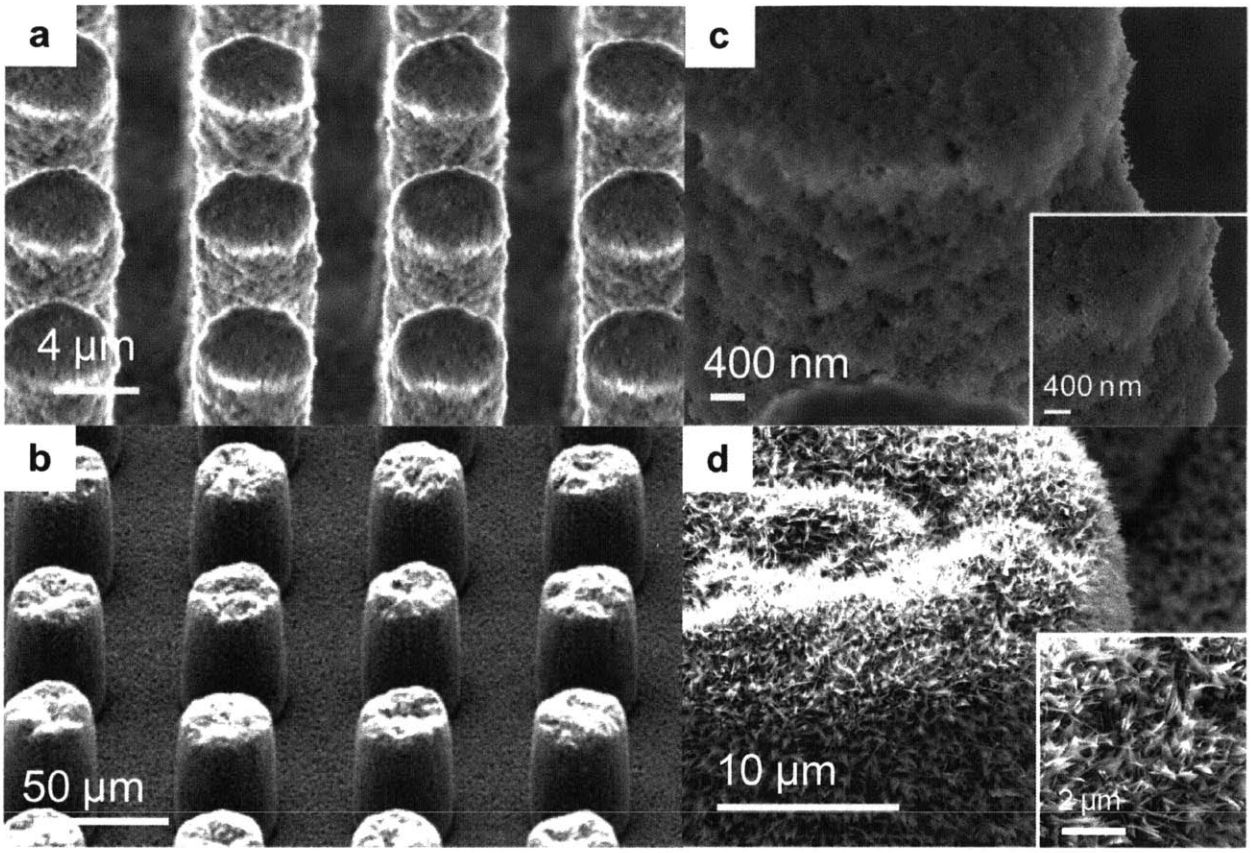

Figure 4-2. Scanning electron micrographs (SEMs) of the representative, fabricated silica and CuO-based hierarchical surfaces. **a**, EPD-coated silica micropillar array and **b**, CuO micropillar array. **c**, magnified view of the silica-based micropillar and EPD-coated SiO_2 nanoparticles (inset). **d**, magnified view of the CuO micropillar and CuO nanostructures formed on the surfaces (inset).

4.4 Surface Characterization

To estimate the surface roughness factors r of the EPD-coated silica and CuO surfaces, we first characterized the roughness factors of the nanoscale structure component, r_n. Detailed surface mophology data of EPD-coated silica and CuO surfaces were obtained by an atomic force microscopy (AFM) on 1 ×1 μm^2 and 5 ×5 μm^2 projected area, respectively, as shown in Fig. 4-3. We used different projected area for two surfaces due to the larger feature size of CuO nanostructures than silica nanoparticles. The roughness factor of the nanoscale structure component, r_n, was calculated as the ratio of the total surface area obtained to the projected area. An average surface roughness factor was obtained with three measurements at different locations. Surface roughness factors (r_n) and the surface rouhgness (RMS) measure by AFM are shown in Table II for the samples with 10 sec and 30 sec EPD coating and CuO. On EPD-coated silica surfaces, root mean squared (RMS) surface roughness increases with increasing deposition time,

but the surface roughness factor decreases at the deposition time of 30 sec. This decrease is due to the disseapearance of asymetric nano-scale structures. In the previous research [115] the mechansims governing nano-sclae and micro-scale structures in EPD was illuminated. The nano-scaled silica nanoparticle features, as shown in Fig. 4-3**a**, **b**, continue to enlarge until micro-scaled features begin to grow, as shown in Fig. 4-3**c**, **d** . Therefore, the surface area is reduced after a specific deposition time even though surface roughness is enhanced. The r_n of CuO measured by AFM is ~1.74 which is, however, to small when we compared with the SEM images of CuO. The large error in AFM measurement on CuO surface is attributed to the complicated feature of CuO nanostructures where the AFM tip cannot skims all the surfaces (Fig. 4-3**e**, **f**).

Figure 4-4 shows the SEMs of the cross section of EPD-coated silica (**a**, **b**) and CuO hierarchical surfaces (**c**) using focused ion beam (FIB). The silica nanostructures formed by 30 sec of EPD coating (Fig. 4-4**b**) has lots of voids while the structures for 10 sec coating shows a more compact layer of silica nanoparticles on the microstructured surfaces (Fig. 4-4**a**). To correctly estimate the roughness factor of the nanoscale structure component r_n, the surface area of voids in Fig. 4-4**b** was calculated using image processing software (ImageJ). The total surface area on the 30 sec, EPD-coated surface is rough twice as large as the surface area measure by AFM. The final surface roughness factors at nanoscale r_n are listed in Table II.

However, the r_n of CuO cannot be simply extracted from the cross section image (Fig. 4-4**c**) because of the deposited byproduct of ablation on the surface during FIB (*i.e.,* the lump on the top of CuO nanostructures in Fig. 4-4**c**). Therefore, we tried to estimate the surface roughness using Wenzel contact angle measurement [117]. The advancing angle of formamide droplets (Molecular biology grade, Sigma) on an Au/thiol-functionalized smooth surface was found to be $\theta_a = 95.3° \pm 1.4°$ ($\theta_r = 90.2° \pm 2.1°$), while the advancing Wenzel angle on the Au/thiol-functionalized CuO nanostructured surface was found to be $\theta_a{}^W = 160.6° \pm 3.2°$ ($\theta_r{}^W = 145.9° \pm 2°$). The Wenzel state was inferred through observation of significant contact angle hysteresis, $\Delta\theta \approx 15°$, in comparison to the Cassie behavior. Using the Wenzel equation, the roughness factor was calculated to be $r_n = 10.2 \pm 2.8$. Note that the r_n based on the contact angle measure only shows the upper bound of the r_n, which may not reflect the true contact condition where vapor bubble is in contact with the surface.

In order to estimate r_n properly, an indirect approach was taken: we extracted the r_n of the CuO nanostructures from CHF data obtained on a nanostructured CuO surface using our CHF model (Eq. 1). We note that the CuO nanostructures on both the smooth and microstructured Cu surfaces were formed using the same oxidation conditions. The total roughness factors, r, were then calculated as the product of r_n and roughness factor of the micropillars r_m (*i.e.,* $r = r_n \times r_m$). Both hierarchical surface types demonstrated superhydrophilic behavior at room temperature due to the large roughness factors obtained, $r > 6$, and the high surface energy of SiO_2 and CuO.

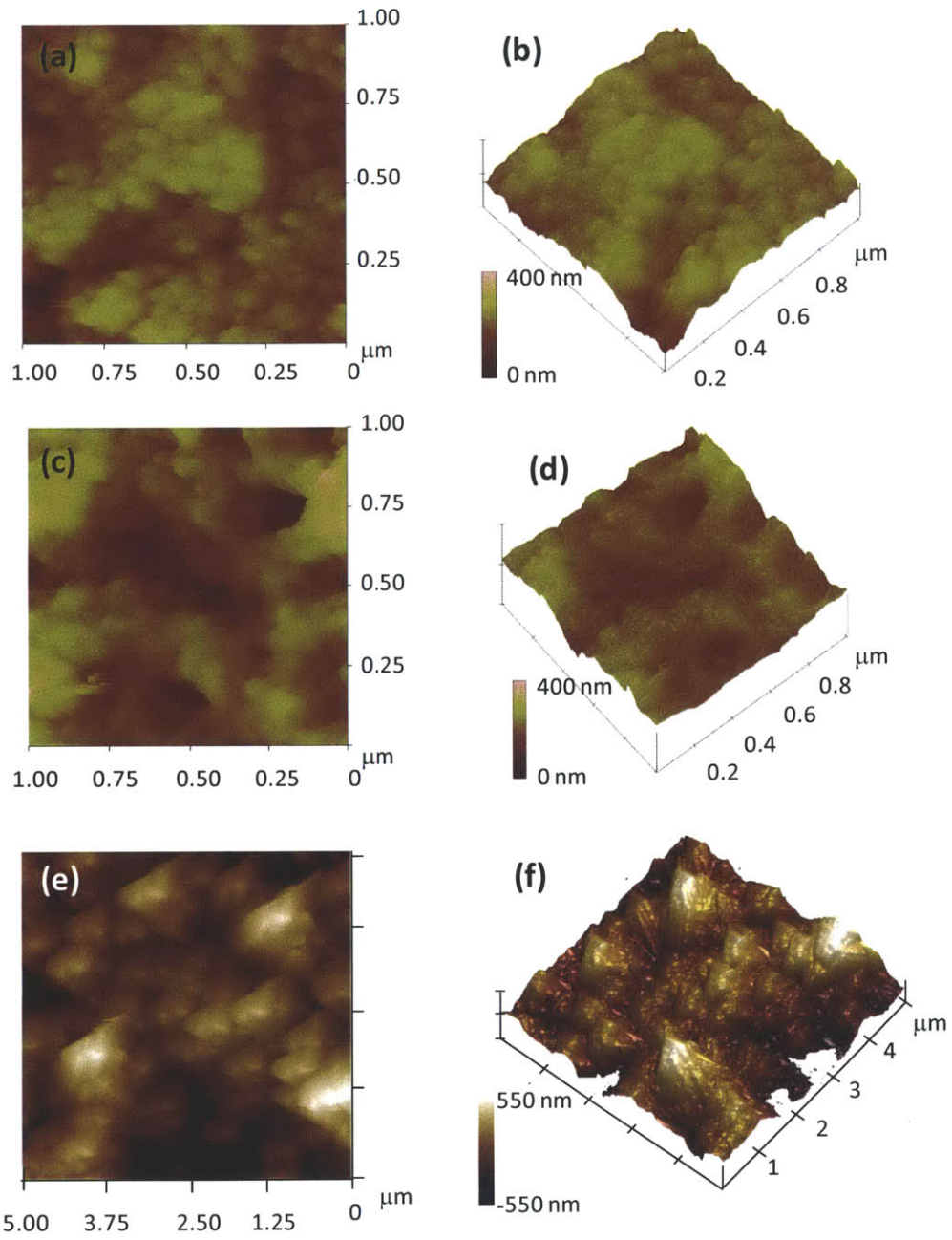

Figure 4-3. Surface molphologies of EPD-coated silica and CuO obtained from atomic force microscopy (AFM) measurements on 1 × 1 μm^2 (**a-d**) and 5 × 5 μm^2 (**e, f**) projected area. The surface features for 10 sec and 30 sec EPD coating are shown in (**a**, **b**) and (**c**, **d**), respectivley and for CuO is shown in (**e**, **f**). The two-deimensional images are (**a**, **c**, **e**), and the three-dimentional images are (**b**, **d**, **f**). Scale bares correspond to the local height of the surface. Nano-scale features composed of silica nanoparticles are observed on the substrate modified by 10 sec of EPD (**a**, **b**). However, the number of nano-scale features decreases at the deposition time of 30 sec and micro-scale structures are observed in (**c**, **d**). The AFM images does not reflect the real surface molphology of CuO surfaces due to the complexity of the structures (**e**, **f**).

Table II. Surface roughness factor r_n, RMS surface roughness and coating thickness of the surfaces coated with silica nanoparticles (14 nm) and CuO. Two EPD surfaces were prepared with two different deposition times (10 sec and 30 sec). The surface roughness factor, by definition, is the ratio of the total surface area to the projected surface area.

Surfaces	EPD-10 sec	EPD-30 sec	CuO
r_n, measured by AFM	1.9	1.8	1.7
r_n, estimated by AFM and cross section image	1.9	3.7	??
RMS (nm), measured by AFM	36	47	241
Coating thickness (nm)	~150	~450	~1000

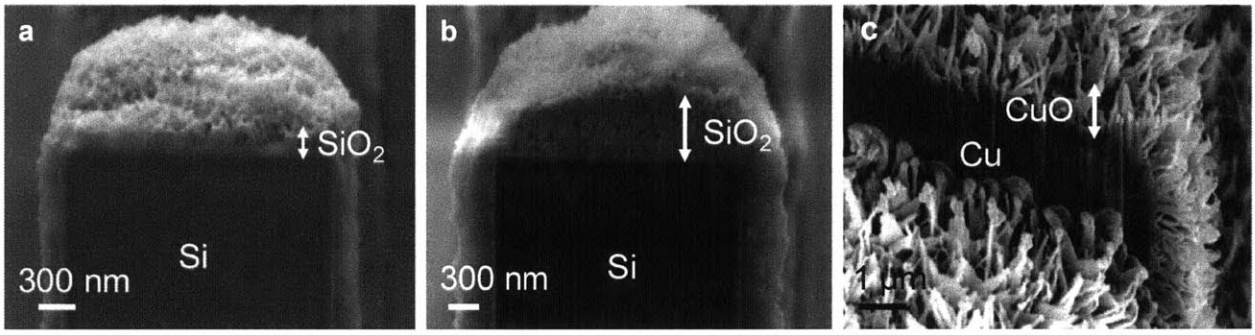

Figure 4-4. SEMs of the cross section of EPD-coated silica (**a**, **b**) and CuO hierarchical surfaces (**c**) using FIB. The thickness of EPD-coated silica layers for 10 sec and 30 sec are ~150 nm and ~450 nm, respectively, while the thickness of CuO layer is ~1 μm. The thicker silica layer in **b** increases the thermal resistance significantly, which decreases the heat transfer coefficient.

We also estimated the thickness of the nanostructure layer using FIB the images (Fig. 4-4). The thickness of EPD-coated silica layers for 10 sec and 30 sec are ~150 nm and ~450 nm, respectively, while the thickness of CuO layer is ~1 μm. The significant increase in the thickness of silica layer imposes higher thermal resistance on the surfaces and decreases the heat transfer.

4.5 Experimental Results

Figure 4-5 shows the heat flux q'' as a function of wall superheat $\Delta T = T_w - T_{sat}$, where T_w is the heated surface temperature and T_{sat} is the saturation temperature (*i.e.*, boiling curve) for the Si/silica- and Cu/CuO-based hierarchical surfaces. Reference boiling curves obtained for smooth SiO_2 surfaces are also shown in Fig. 4-5 for comparison. Details of the tested surface geometries are listed in Table II. The maximum uncertainty of the heat flux and temperature measurements was calculated to be ~5.6% and ±1.8 K, respectively [118]. While a CHF of ~83 W/cm^2 was obtained on the smooth SiO_2 (Sm) surfaces, CHF values of 236 W/cm^2 and 249.2 W/cm^2 were demonstrated on the best performing Si/silica (EPD-Hier3) and Cu/CuO-based (CuO-Hier3)

hierarchical surfaces, respectively. The significant enhancement in CHF on the hierarchical surfaces (up to 200%) is attributed to the high surface roughness factor, which provides a large surface force to balance the momentum force due to evaporation [113]. In addition, the sudden reduction in superheat ΔT along the boiling curve of hierarchical surfaces (*i.e.*, "kickback") is indicative of nucleation sites within nanostructures becoming active [119]. The high roughness factor of nanostructured surfaces on the sample EPD-Hier3 results from the thick deposited silica layer which, however, leads to the high thermal resistance. While similar characteristics are shown in all the other boiling curves of the hierarchical surfaces, the boiling curve of the sample EPD-Hier3 demonstrates a low slope and the high superheat ($\Delta T \approx 68$ °C) due to the thick SiO_2 nanoparticle layer.

TABLE II: Geometric parameters of the hierarchical surfaces. The units of height, diameter and (center-to-center) spacing for micropillars are in microns. The roughness factor of contact line, r, the products of roughness ratios at micro and nanoscales, *i.e.*, $r = r_m \times r_n$.

Sample No.	Height (h)	Diameter (d)	Spacing(s)	r_m	r_n	r
Sm	n/a	n/a	n/a	1.0	1.0	1.0
EPD-Hier1	20	10	15	2.01	1.9	3.8
EPD-Hier2	20	10	5	3.79	1.9	7.2
EPD-Hier3	20	5	10	2.40	3.7	8.9
CuO	n/a	n/a	n/a	1.0	4.8*	4.8
CuO-Hier1	35	30	30	1.91	4.8*	9.2
CuO-Hier2	61	30	30	2.59	4.8*	12.4
CuO-Hier3	68	35	30	2.78	4.8*	13.3

*Approximation based on the CHF model and experimental CHF values on CuO nanostructured surfaces

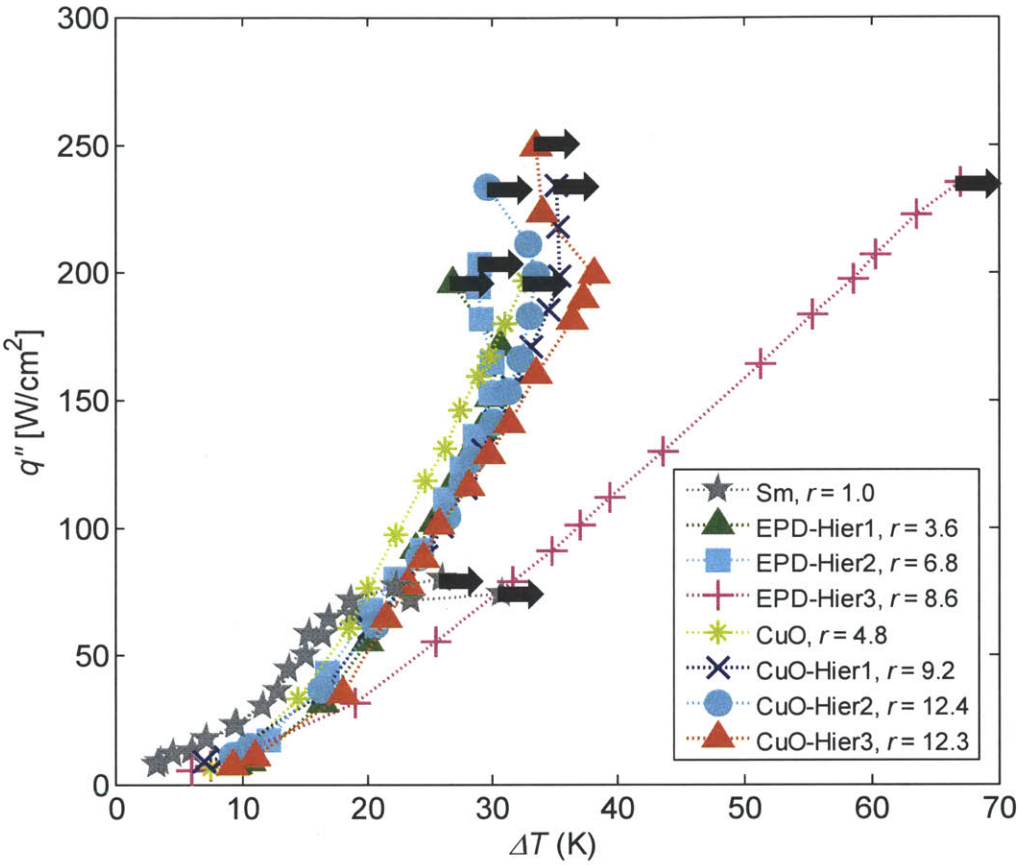

Figure 4-5. Boiling curves on the smooth (r = 1) and hierarchical (r > 1) surfaces detailed in Table II. The arrows indicate the CHF condition. The consistency and accuracy of the measurements are demonstrated by the two nearly identical boiling curves for the smooth surface. The boiling curves show a clear trend of increasing CHF with surface roughness due to roughness-augmented capillary forces.

In Fig. 4-6, the predicted CHF as a function of α (Eq. 1) is overlaid with data from our experiments for the hierarchical surfaces (in red) and previously tested microstructured surfaces[113] (in blue). The dash line represents the CHF predicted by the classical Kutateladze-Zuber (K-Z) model [21, 22] (hydrodynamic instability mechanism) using an empirical factor of K = 0.18 in Eq. 1 [105] plotted for comparison. The good agreement between the data and model, which does not contain any fitting parameters, for α ranging from 1 to ~14 demonstrates the validity of the model for the structured surfaces in complete wetting regime. The trend increasing CHF with increasing surface roughness is well-captured by the model which suggests that the key physics of the CHF mechanism on these structured surfaces are accounted for. While the value of r_n on CuO surfaces was approximated based on the CHF model and experimental data of CuO nanostructured surfaces, the agreement between the CHF on CuO hierarchical surfaces

(CuO-Hier1-3) and model prediction suggests that the effective surface roughness pinning the vapor bubble is ~4.8 on our CuO nanostructured surfaces.

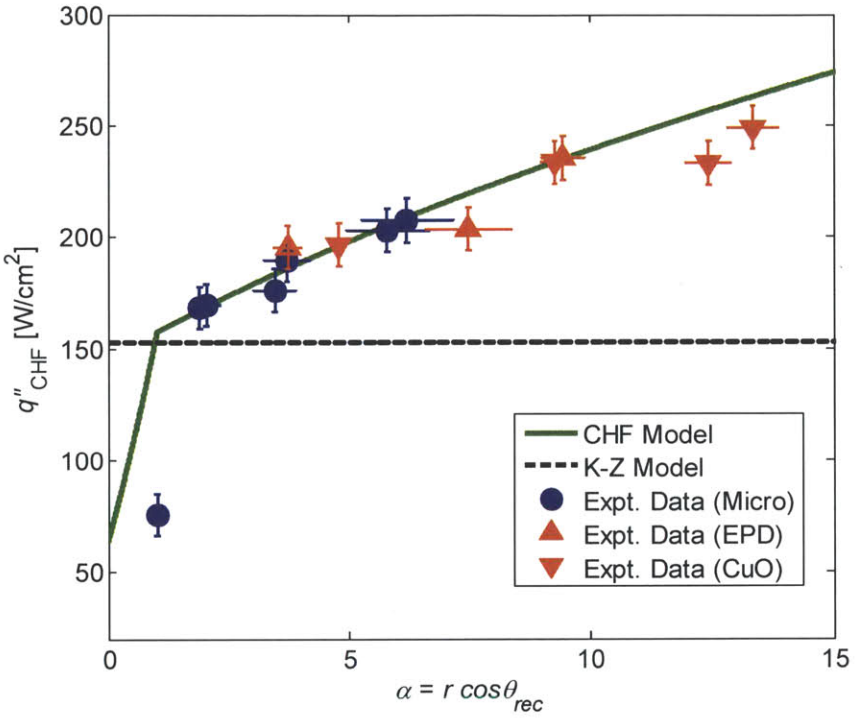

Figure 4-6. CHF as function of α $(= r\cos\theta_{rec})$. The proposed model (solid line) is compared to the K-Z model with a factor of $K = 0.18$ (dashed line). The symbols show the CHF data for (●) microstructured surfaces (see Ref. 8), and (▲) EPD-coated SiO_2 and (▼) CuO hierarchical surfaces, as a function of the estimated α values.

4.6 Conclusion

In conclusion, we fabricated hierarchically-structured surfaces using electrophoretic deposition on microstructuring silicon, and electroplated and oxidized copper with roughness factor, r of 3.6 – 13.3 to investigate the CHF conditions on high roughness factor surfaces in pool boiling. The excellent agreement between the CHF model and experimental observations on the hierarchical surfaces indicates that the roughness-amplified surface force plays the defining role in CHF enhancement on structured surfaces with roughness factor r ranging from 1 to ~14. CHF of 249.2 W/cm^2 (*i.e.*, a ~200% CHF enhancement compared to smooth SiO_2 surfaces), achieved on CuO-based hierarchical surfaces, demonstrates high heat removal capability. This scalable fabrication process by electroplating copper micropillars and simple chemical oxidation process promises an exciting opportunity for a new method to achieve high performance boiling heat transfer.

Chapter 5 Two-Phase Microchannel Heat Sinks

5.1 Introduction

The increasing power consumption within the confined size of modern integrated circuits (ICs) has made thermal management the bottleneck for further development and progress of the electronics industry [15, 91]. For example, John Thome, in a 2006 editorial, suggested that ICs may require over 300 W/cm^2 of power removal in the next few years[14]. In addition, the thermal management demands of specialty applications such as concentrated photovoltaics, power electronics, and laser diode can be over 1000 W/cm^2 [18, 19, 90]; and the need for thermal management schemes capable of dissipating such high heat fluxes at uniform temperature environments and with low temperature rises has been well-recognized. Two-phase microchannel heat sinks, where the latent heat of vaporization offers an efficient method to dissipate large heat fluxes in a compact device and the large surface to volume ratio provides lower thermal resistance than its macroscale counterpart [36-38], has been considered as a promising solution to address the challenge in high-flux heat dissipation and uniformly temperature control for various electronic devices. However, at length scales where surface tension dominates the shape of an interface (i.e., much lower than the capillary length), the rapid expansion of vapor bubble occupies the space of microchannel before it can depart from the heating surface, leading to large pressure fluctuations in the flow channels [42-46] (*i.e.,* instability) and dry out during boiling which, severely limits the heat removal efficiency of two-phase microchannel heat sinks. Therefore, recent studies have focused on using microstructures, such as inlet restrictors [49], reentrant cavities [51, 52], and nanowire-coated surface [56] integrated into the microchannel, to mitigate the flow instability and to enhance heat transfer. While the previous studies attribute the reduction in instabilities due to pressure regulation [49, 50] and an increase in nucleation density [51, 54, 56, 57], the approach to manipulate bubble dynamics using the surfaces has never been achieved. Meanwhile, the precise role of capillary-length-scale surface structures on the flow instability is not well-understood. In this study, we propose a design for a microchannel with well-defined microstructured surfaces to systematically investigate the role of surface topology on flow instability and characterize the performance of the microchannels with a custom closed loop test setup. The preliminary data shows that the device is capable to dissipate heat fluxes of ~508 W/cm^2 with mass flux of ~1530 kg/m^2 s.

5.2 Microstructured Surfaces and Two-Phase Microchannel Heat Sinks

To investigate the effect of surface structure on flow instability, silicon micropillars with heights of 25 μm, diameters of 10 μm and pitch of 25-45 μm were integrated into microchannels of 10 mm (length) × 500 μm (width) × 500 μm (height), as shown in Fig. 5-1. The fabrication process is shown in Fig. 5-2, following: (1) Si micropillar array were created on Si substrate using deep reactive ion etching (DRIE). (2) A layer of 500 μm Si was etched through using DRIE to define the channel. The layer was then bonded onto the Si substrate with Si micropillars

with fusion bonding. (3) A SiO_2 layer was grown on the surface of Si micropillars and microchannel. A Pyrex glass with through holes made by laser drilling was bonded onto Si using anodic bonding to create the microchannel. (4) Finally, a layer of 250 nm thick Platinum (Pt) was deposited on the backside of the channel with E-beam evaporator and patterned by lift-off technique to serve as heater (8 mm long × 250 μm wide) and temperature sensors. Figure 3 shows scanning electron micrographs (SEMs) of cross section view of the microchannel with representative microstructures fabricated for this study and the magnified view of microstructured surfaces on the channel bottom is shown in the inset of Fig. 5-3. Detailed surface geometries are listed in Table III. The microstructures with different geometries were designed for testing various solid fraction φ, roughness factor r (*i.e.*, r = total surface area/projected surface area), and permeability [98, 120] γ^2 effects on the vapor bubble dynamics in two-phase flows. In addition, to correctly calculate the heat flux, q'', into the channel by the integrated heater on the backside, we simulated the heat flux distribution using finite element software, COMSOL. Roughly 50% of the heat conducts through the bottom surface while other 50% conducts from the side wall of channel based on the simulation results. Therefore, the total surface area using to calculate heat flux is 8 mm × 1 mm.

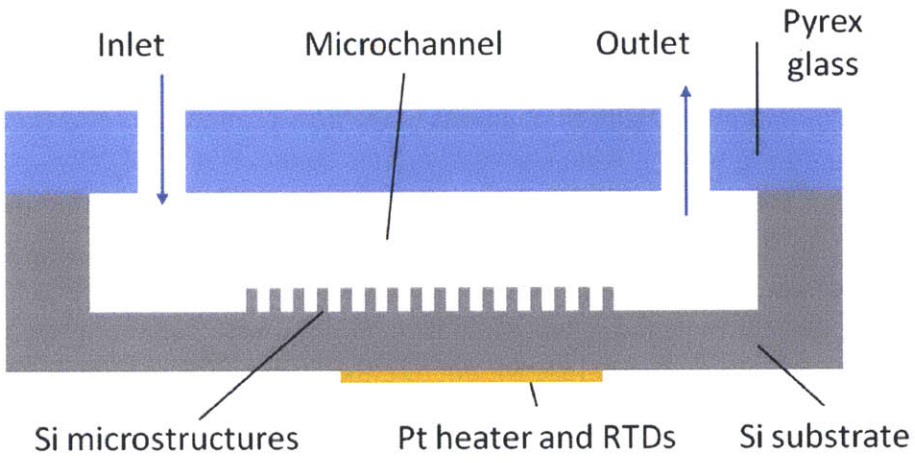

Figure 5-1. Schematics of the microchannel design. The microchannel has length of 10 mm, width of 500 μm, and height of 500 μm. The micropillars incorporated into the microchannel were etched out of Si with heights of 25 μm, diameters of 10 μm and pitch of 25-45 μm. The 8 mm (length) × 250 μm (width) Platinum (Pt) heater and four resistance temperature detectors (RTDs) were fabricated along the microchannel on the backside.

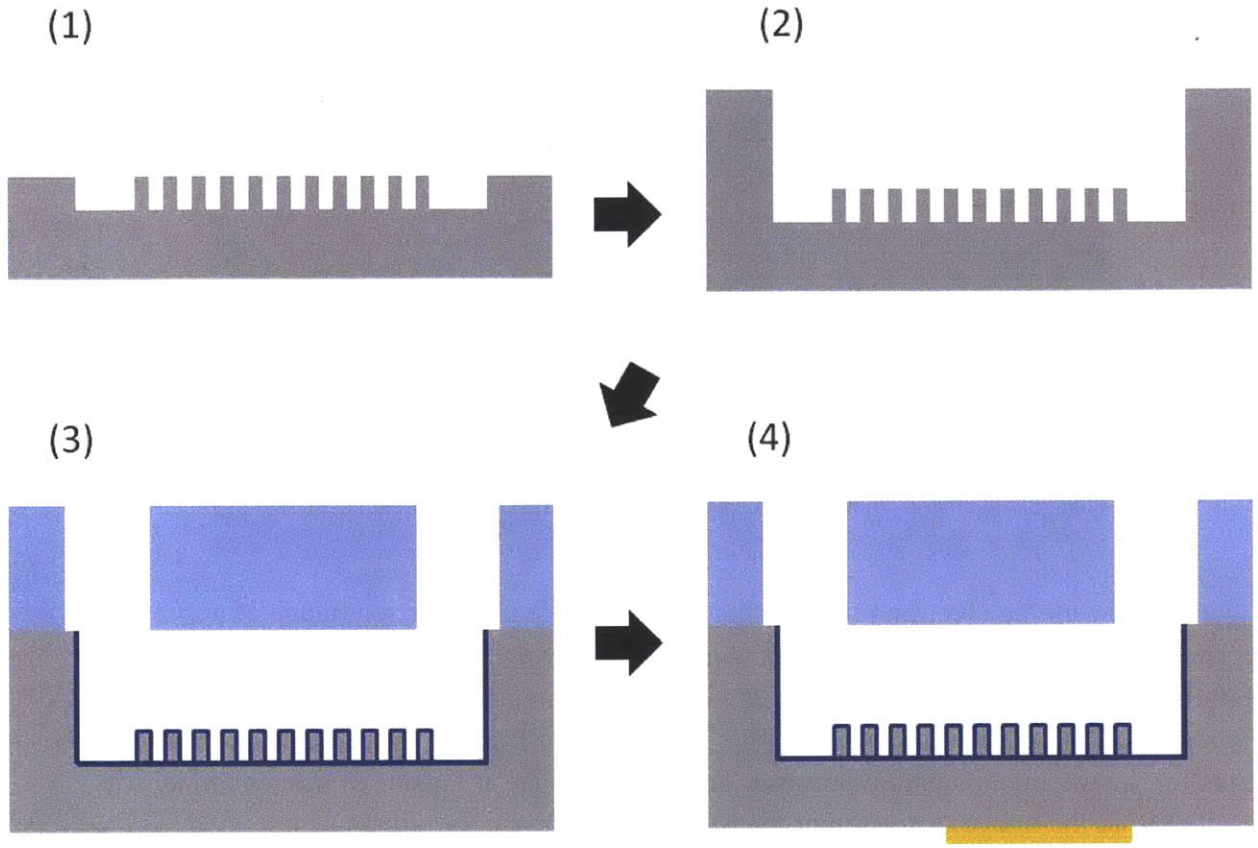

Figure 5-2. Fabrication processes of the two-phase microchannel. (1) Micropillars of 25 μm height were etched out Si using DRIE. (2) A 500 μm thick Si wafer was etched through using DRIE and then bonded onto the wafer with micropillar array using Si-Si fusion bonding (3) After the Si wafer bonding, a 100 nm thick SiO_2 layer was grown on the surfaces and then a 500 μm thick Pyrex glass wafer with the inlet and outlet holes was bonded onto the Si wafers as a cover to form a microchannel. (4) A 250 nm thick Pt layer was deposited on the backside of the microchannel using e-beam evaporation and patterned to form heater and temperature sensors.

TABLE III: Geometric parameters of the microstructures. The units of height, diameter and pitch for micropillars are in microns and the unit of permeability is meter square. The solid fraction, φ, and roughness factor, r, are calculated by: $\varphi = (\pi d^2/4)/l^2$ and $r = 1 + \pi d\, h(\pi/2)/l^2$, respectively. The permeability, γ^{-2}, is calculated based on Sangani and Acrivos[120].

Sample No.	Height (h)	Diameter(d)	Pitch(l)	d/l	φ	r	γ^{-2}
M1	25	10	25	0.4	0.126	2.26	2.06×10^{-11}
M2	25	10	30	0.333	0.087	2.05	4.03×10^{-11}
M3	25	10	45	0.222	0.012	1.70	1.49×10^{-10}

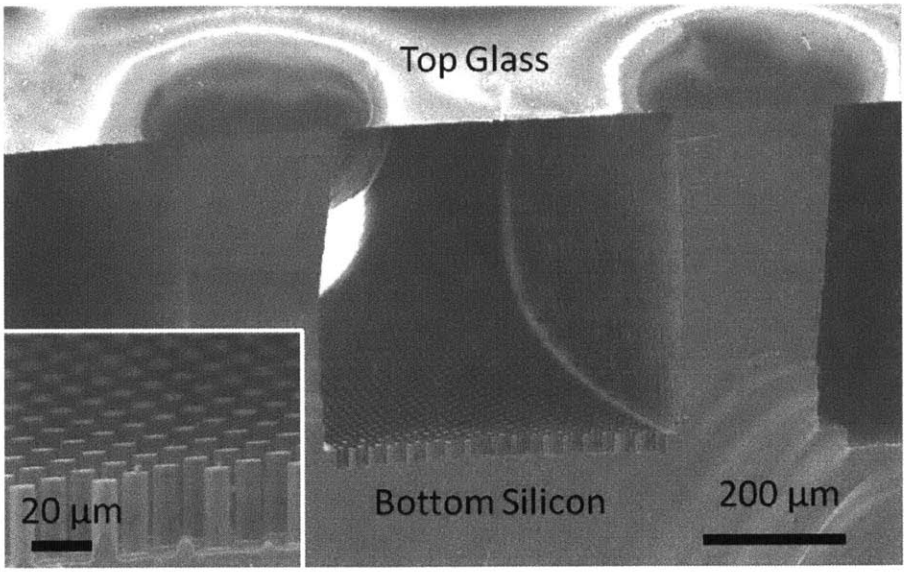

Figure 5-3. Scanning electron micrographs (SEMs) of the cross section image of a representative, fabricated microchannel and magnified view of micropillars on the channel bottom surface (inset). The channel with width of 500 μm and height of 500 μm was fabricated using wafer bonding and DRIE. Two chambers next to the center microchannel are made for the thermal insulation purpose. The curved image at far side of microchannel was resulted from the image distortion of the SEM.

5.3 Experimental Setup

A closed loop test setup shown in Fig. 5-4 was used for two-phase heat transfer experiments. A custom fixture was designed to interface the loop pipe and microchannel, and hold the sample onto the microscope for two-phase phenomena observation. For all tests, high purity water (CHROMASOLV for HPLC, Sigma-Aldrich) was first de-gassed within the degassing chamber by heating up to 120 °C, and then pumped through the closed loop using peristaltic pump. All the data, including flowrate, pressure drop across the microchannel, and temperature along the channel were recorded using LabVIEW software. The conduction heat loss on the testing setup was characterized by heating up the sample to ~140 °C without water in the channel. During the experiment, the inlet temperature was maintained to be ~1 °C below the saturation temperature to avoid any single phase cooling effect.

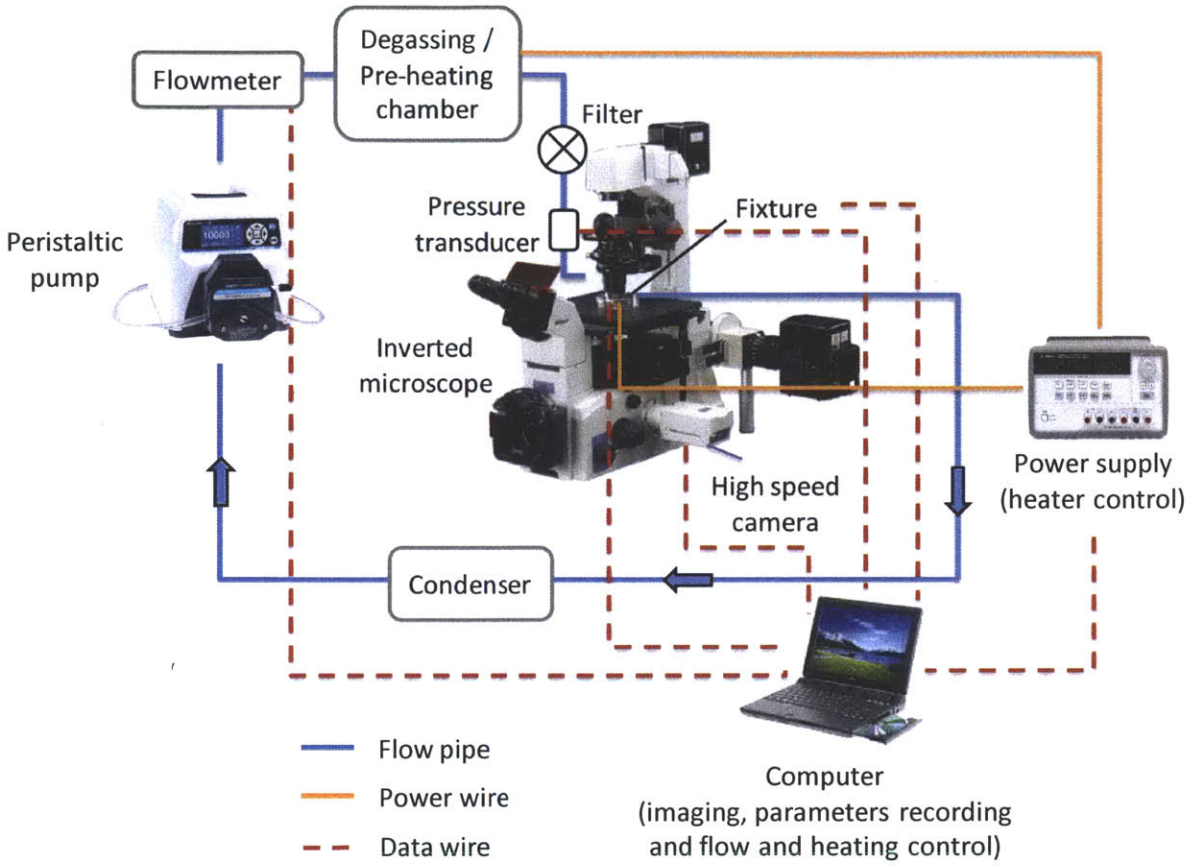

Figure 5-4. Custom closed loop system for the two-phase flow experiment. The flow was pumped through the microchannel and the whole loop using a peristaltic pump. The flow was preheated to 1 °C less than saturation temperature in the preheating chamber. A customized fixture was made to interface between the loop pipes and microchannel and hold onto the inverted microscope to observe two-phase phenomena. The two-phase flow was then cooled down to ~60 °C after the condenser. All the data, including water mass flux, pressure drop across the microchannel, and temperatures along microchannel were recorded with LabVIEW.

5.4 Experimental Results

Figure 5-5 shows time lapse images of typical two-phase phenomena in the microchannel under various heat flux q'' conditions with the sample M3. The onset of nucleation boiling (ONB) was observed at a heat flux, $q'' \approx 22$ W/cm^2 (Fig. 5-5**a**). The elongated bubble was formed with increasing heat flux (Fig. 5-5**b**) and finally, slug flow was reached [119] with heat flux, $q'' \approx 508$ W/cm^2 (Fig. 5-5**c**). However, the vapor quality under this condition (*i.e.*, $q'' \approx 508$ W/cm^2) is ~0.05 due to the high mass flux ($G \approx 1530$ kg/m^2 s). Therefore, the temperature and pressure fluctuations are not significant.

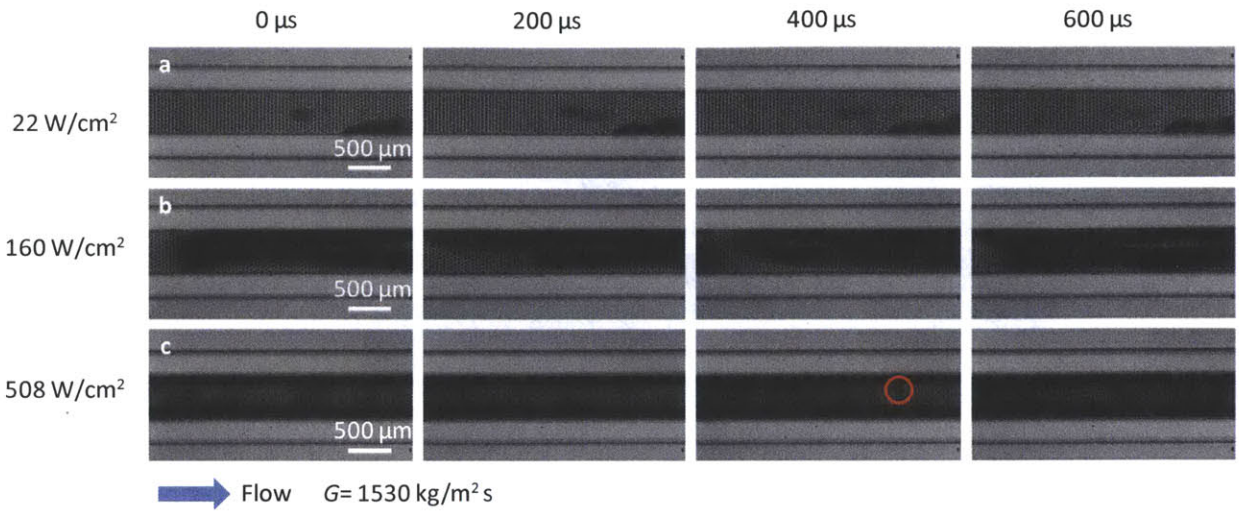

Figure 5-5. Time lapse images of two-phase phenomena with various heat fluxes: **a**, 22 W/cm^2, **b**, 160 W/cm^2 and **c**, 508 W/cm^2. **a**, Onset of nucleation boiling (ONB) was observed. The vapor bubble nucleated both on the top of structured surfaces and microchannel side wall. **b**, The elongated bubble was formed with increasing heat flux. **c**, A long, single bubble was obtained in the channel. However, the bubble nucleation observed on the top of the micropillars (highlighted by the red circle) demonstrated that the channel reached slug flow.

Figure 5-6 and 5-7 show the heat flux q'' as a function of wall superheat $\Delta T = T_w - T_{sat,}$ where T_w is the averaged surface temperature and T_{sat} is the saturation temperature (*i.e.*, boiling curve) and the heat transfer coefficient h as a function of heat flux q'', respectively. The sudden reduction in superheat ΔT along the boiling curve of hierarchical surfaces (*i.e.*, "kickback") is indicative of nucleation sites within the micropillars becoming active [119]. Note that the CHF condition was not achieved in the experiments. The end of boiling curves indicates the burnout of the backside heaters due to the fabrication defects. A heat flux, $q'' \approx 508$ W/cm^2 and the heat transfer coefficient, $h \approx 2\times10^5$ W/m^2 K, were demonstrated on sample M3. The results seemingly show the positive correlation between the heat transfer performance and structure permeability γ^{-2}.

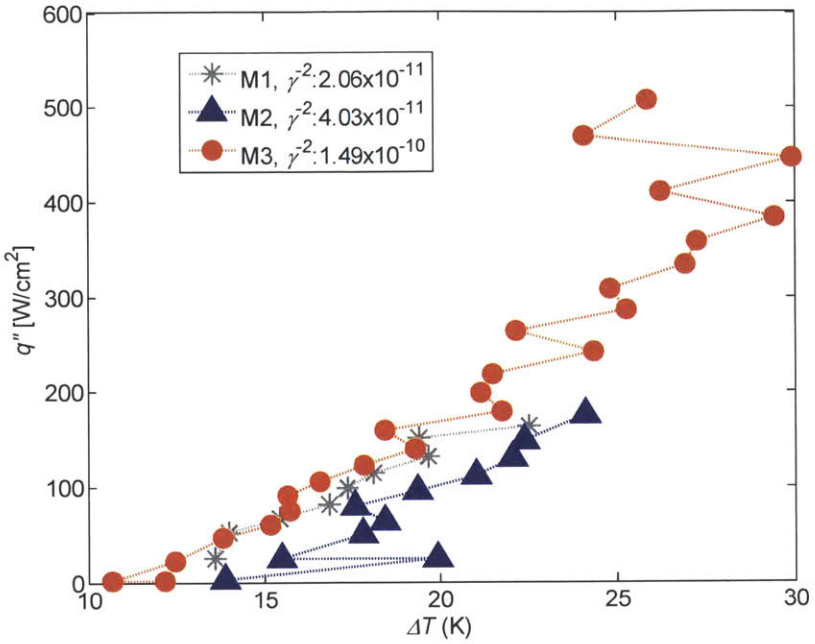

Figure 5-6. Boiling curves on the surfaces detailed in Table III. The "kickback" phenomenon shows the nucleation occurs on the structured surfaces. CHF was not reached due to the burnout of heaters.

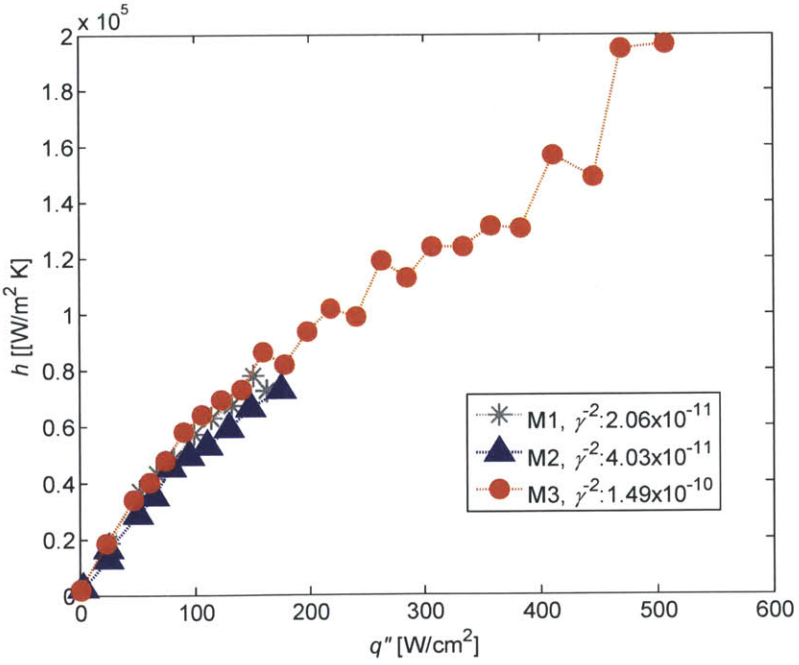

Figure 5-7. Heat transfer coefficient h as function of heat flux q". Heat transfer coefficient, $h \approx 2\times10^5$ W/m^2 K, were obtained on sample M3. The permeability of the structured surface shows a positive effect on the heat transfer performance.

5.5 Conclusion

In this study, we demonstrate the design of a two-phase microchannel incorporated with microstructured surfaces, and backside heater and temperature sensors, used as a platform for systematically studying surface geometry effects on bubble dynamics in two-phase flow. The preliminary experimental data shows a significant heat dissipation capability ($q'' \approx 508$ W/cm^2 and $h \approx 2\times10^5$ W/m^2 K). The positive correlation between the heat transfer performance and permeability of the microstructures support the idea of using structured surface to mitigate flow instability and enhance heat transfer performance. The insight gained from this study provides an exciting opportunity to design two-phase microchannel heat sinks for high heat flux thermal management applications.

5.6 Future Works

For the future study in the surface geometry effects on flow instability, we plan to achieve following points:

1. Reduce the mass flux (flowrate): Flow instabilities are usually observed when the vapor quality is higher than 0.2 and Weber's number is less than 1, which requires the mass flux in the current microchannel geometry to be less than 500 kg/m^2 s (i.e., $G < 500$ kg/m^2 s). While the minimal mass flux of current pump is ~1530 kg/m^2 s, to further study the surface structure effects on flow instabilities, the power of the peristaltic pump has to decrease.

2. Microchannels with smooth surfaces: To understand the surface structure effects and study the enhancement in heat transfer due to the structured surfaces in two-phase microchannel heat sinks, the baseline of flow behaviors and heat transfer characteristics under the same heating conditions have to be established. Therefore, the microchannels with the same dimensions but smooth surfaces are required.

3. Wide range of surface permeabilities: Our preliminary results show a positive correlation between heat transfer performance and the permeability of the microstructures. However, the result is inconclusive due to the small range of the permeabilities of the current structure design. A wide range of structure permeabilities are needed to validate this hypothesis.

Chapter 6 Future Directions and Perspective

6.1 Summary of Work

Two-phase microchannel heat sinks have been recognized as a potential approach to address the challenge in high heat flux thermal management due to the high latent heat of evaporation. However, the flow instability problem associated with insufficient bubble removal hinders the practical implement of the two-phase microchannel. To solve this problem, this thesis is focused on manipulation of vapor bubble dynamics to enhance the bubble departure using structured surfaces.

We first demonstrated that on structured surfaces with asymmetry the liquid spreading direction can be manipulated. The deflected nanopillars due to the thermal residual stress create energy barrier in all directions but one, leading to the uni-directional liquid spreading (*i.e.*, liquid spreads in one direction only). We developed a geometrical model based on surface energy minimization shows an excellent agreement with the experimental results. The insight gained from this research provides a guideline to achieve the fine control on the liquid behaviors using surface structure design, which potentially can be applied to manipulate vapor bubble behavior.

The surface structure effect on heat transfer performance in pool boiling condition was then investigated. Well-designed microstructured surfaces with wide-range of surface roughness factors ($r = 1 \sim 6$) were fabricated to study the role of capillary-length-scale surface roughness on critical heat flux (CHF). We were able to achieve CHF of ~200 W/cm^2 with microstructured surface only. In addition, the CHF enhancement was found to be well-correlated with the surface roughness factor. A model was developed based on force balance argument and roughness-amplified surface tension and an excellent agreement between the model and experimental data was found.

We subsequently fabricated nano- and hierarchically structured surfaces with high roughness factor ($3 < r < 14$), and a CHF of ~250 W/cm^2 was demonstrated on the surface with highest roughness factor ($r \approx 13.3$). The CHF data on the hierarchical surfaces also shows good agreement with the CHF prediction by the analytic force balance model. The study demonstrates the important effect of surface roughness at capillary length scale on enhancing CHF.

Finally, a two-phase microchannel incorporated with microstructured surfaces, and backside heater and temperature sensors, used as a platform for systematically studying surface geometry effects on bubble dynamics in two-phase flow, was designed and fabricated. Our experimental results show that we are able to achieve heat flux $q'' \approx 508$ W/cm^2 and heat transfer coefficient $h \approx 2\times10^5$ W/m^2 K with mass flux $G \approx 1530$ kg/m^2 s. A positive correlation between the heat transfer performance and permeability of the microstructures was found, which supports the hypothesis that structured surface can manipulate bubble dynamics to reduce flow instability.

This exciting finding from the preliminary result demonstrates the great potential for the new design of two-phase microhcannel heat sinks to address the flow instability challenge.

6.2 Future Directions

We envision the work in this thesis can be extended in following aspects in the future.

For manipulation of liquid spreading, we proposed to achieve real-time control of liquid spreading direction on-demand using electrowetting phenomenon. In Chapter 2, we tailored the polymers to ensure that the imbibition condition can be satisfied and the spreading occurred spontaneously after the droplet was deposited onto the surface [121]. However, if the contact angle of liquid is larger than the imbibition angle, no spreading can occur (*i.e.*, no spreading region in Fig. 2-6 and Fig. 2-7). Electrowetting is a well-known phenomenon that involves modifying the wettability and the contact angle of a liquid (electrolyte) on the surface using an electric potential [8, 122, 123]. Therefore, even if the contact angle is in no spreading region, we can reduce the liquid contact angle by applying the electric potential across the droplet and surface and allow spreading occurring as shown in Fig. 6-1.

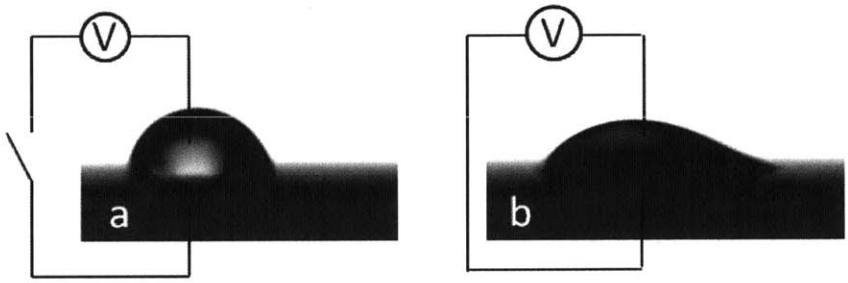

Figure 6-1. Real time control of liquid spreading on demand using electrowetting. **a**, Before the electric potential is applied, the contact angle of liquid is above imbibitions angle and no spreading occurs. **b**, After the electric potential is applied across the droplet and surface, liquid contact angle is decreased to smaller than imbibitions angle and uni-directional spreading can occur on the asymmetric nanostructured surfaces.

Furthermore, the symmetric spreading (*i.e.*, spreading in all directions) can occur on the asymmetric nanostructured surfaces if the contact angle is in bi-directional spreading region when higher electric potential is applied. Using electrowetting and the asymmetric nanostructured surfaces, we can achieve real-time manipulation of liquid spreading behaviors between no spreading, uni-directional spreading, and symmetric spreading.

For CHF enhancement using structured surfaces, the further study and validation for the CHF mechanism is suggested. The high-speed, infrared thermometry technique as shown in Fig. 6-2 [103] allows us to observe the contact line movement of vapor bubble during bubble growth and departure. Therefore, we can study contact line pining and de-pining, bubble departure radius, nucleation site density, and local superheat.

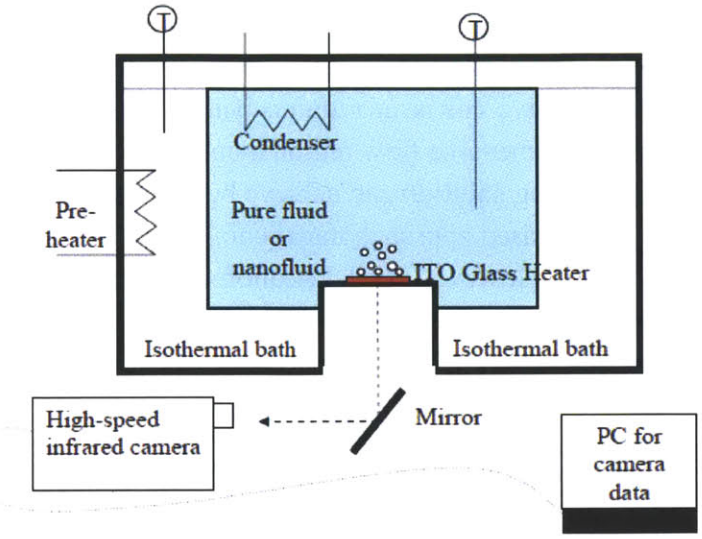

Figure 6-2. Pool boiling facility with infrared thermometry and high speed video cameras [103].

For two-phase microchannel heat sinks, in addition to the future works listed in section 5.6, we proposed to introduce asymmetric structured surfaces into the microchannel in the future, as shown in Fig. 6-3. The asymmetric structured surfaces can alter force balance acting on the vapor bubble and allow bubble depicturing preferentially in certain direction. This directional departure can prevent vapor bubble from growing toward inlet of the channel and, as result, mitigate flow instabilities.

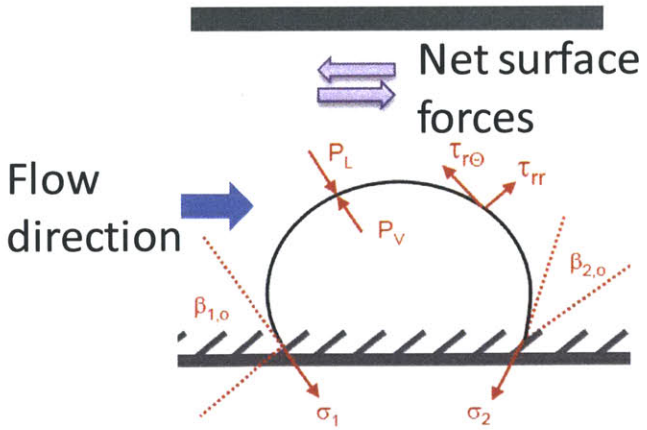

Figure 6-3. Vapor bubble on asymmetric structured surfaces in microchannel.

6.3 Perspectives

In the practical implementation of two-phase microchannel heat sinks, another problem is to maintain the uniform flow when a multi-channel system is introduced. The vapor bubble nucleation significantly increases local flow resistance and reduces the flow through the

microchannel, leading to dry-out problem due to the insufficient liquid supply. The positive feedback loop imposes a great challenge in controlling the heat transfer performance for two-phase microchannel heat sinks. To solve this issue requires better fundamental understanding of two-phase flow phenomena, a comprehensive flow region map, and active/passive feedback control system. In addition, the cooling solution can achieve better performance when it is close to the heat sources. Therefore, the desired approach may be to imbed the microchannel into the substrate of the Si-based electronics. However, the fabrication compatibility can be a big and expensive issue. Another approach is to introduce the channel at the packaging level which, again, requires more study and development in the material selection and fabrication process. For the system level, the challenge in practical implementation of liquid cooling is the interface to introduce liquid into the microchannel. The liquid pipeline has to be integrated onto the circuit board and the interface between the pipeline and liquid source needs a proper and elaborate design for the simple, robust, and replace-easy setup.

For a broader perspective, the wide spectrum of applications in electronics imposes very different problems in thermal management. While performance-orientated electronics, such as CPU for servers, requires high heat dissipation capability, mobile devices consuming less power need a quiet, light, and low power consumption cooling solution. Also, the fine temperature control for photonic devices is another severe problem.

To address these issues, we envision the several research directions in thermal management in the future to include:

1. Fundamental study of solid state physics for the electronics. To solve the problems in electronics cooling, a better understanding in the physics of heat generation and transfer is required.
2. Multi-scale and multi-physics simulation techniques. The heat transfer phenomena in most electronics is complicated and across a wide range of length scale. Better simulation tools are needed to provide a quick and accurate estimation of thermal situation in the electronics.
3. Better understanding into intermolecular interaction. The micro/nanostructures have a great effect on heat transfer performance, especially involving phase change. A study in the interaction between the liquid and solid phases can provide an improved understanding in enhancing the liquid properties for better heat transfer.
4. Synthetic materials for enhancing thermal conductivity. The best material for heat conduction is diamond ($k \approx 2200$ W/m·K). Given the rarity and price of diamond, the material with high thermal conductivity and low cost is needed for better thermal management purposes.

Thermal management has been one of the most important issues for the progress of electronic industry. The thermal issue has to be taken into account at early stage of designing the electronic chips. Furthermore, energy has become another critical issue in the modern world, given the fact

that oil price is expected to go up continuously. These challenges require great efforts in heat transfer research to improve the technology. Therefore, we anticipate that there will be even more research and development invested in the heat transfer area in the near future.

References

1. Feynman, R.P., *There's Plenty of Room at the Bottom.* Journal of Microelectromechanical Systems, 1959. **1**(1): p. 60-66.
2. Hornbeck, L.J., et al., *Digital micromirror device-commercialization of a massively parallel.* Microelectronic Systems, 1997. **62**: p. 3-8.
3. Kovacs, G.T., *Micromachined Transducers Sourcebook.* 1st ed. 1998 McGraw-Hill Science.
4. Wenzel, R.N., *Resistance of Solid Surfaces to Wetting by Water.* Ind. Eng. Chem., 1936. **28**(8): p. 988–994.
5. Cassie, A.B.D. and S. Baxter, *Wettability of porous surfaces.* Transactions of the Faraday Society, 1944. **40**: p. 0546-0550.
6. Bico, J., U. Thiele, and D. Quéré, *Wetting of textured surfaces.* Colloids and Surfaces A: Physicochemical and Engineering Aspects, 2002. **206**(1–3): p. 41-46.
7. Chiou, N.R., et al., *Growth and alignment of polyaniline nanofibres with superhydrophobic, superhydrophilic and other properties.* Nature Nanotechnology, 2007. **2**(6): p. 354-357.
8. Krupenkin, T.N., et al., *From rolling ball to complete wetting: the dynamic tuning of liquids on nanostructured surfaces.* Langmuir, 2004. **20**(10): p. 3824-3827.
9. Cebeci, F.Ç., et al., *Nanoporosity-driven superhydrophilicity: a means to create multifunctional antifogging coatings.* Langmuir, 2006. **22**(6): p. 2856-2862.
10. Garrod, R., et al., *Mimicking a stenocara beetle's back for microcondensation using plasmachemical patterned superhydrophobic-superhydrophilic surfaces.* Langmuir, 2007. **23**(2): p. 689-693.
11. Quéré, D., *Non-sticking drops.* Reports on Progress in Physics, 2005. **68**(11): p. 2495.
12. Extrand, C., et al., *Superwetting of structured surfaces.* Langmuir, 2007. **23**(17): p. 8882-8890.
13. Wang, J., et al., *Dewetting of conducting polymer inkjet droplets on patterned surfaces.* Nature materials, 2004. **3**(3): p. 171-176.
14. Thome, J.R., *The New Frontier in Heat Transfer: Microscale and Nanoscale Technologies.* Heat Transfer Eng., 2006. **27**(9): p. 1-3.
15. Pop, E., *Energy dissipation and transport in nanoscale devices.* Nano Res., 2010. **3**: p. 147–169.
16. Thome, J.R., *The New Frontier in Heat Transfer: Microscale and Nanoscale Technologies.* Heat Transfer Engineering, 2006. **27**(9): p. 1-3.
17. Price, D.C., *A review of selected thermal management solutions for military electronic systems.* IEEE Transactions on Components and Packaging Technologies, 2003. **26**(1): p. 26-39.
18. Roadmap, I., *International Technology Roadmap for Semiconductors, 2009 edn.* Executive Summary. Semiconductor Industry Association, 2009.
19. Krishnan, S., et al., *Towards a thermal Moore's law. Advanced Packaging.* IEEE Transactions on Advanced Packaging, 2007. **30**(3): p. 462-474.
20. Pautsch, G., *Thermal Challenges in the Next Generation of Supercomputers.* Proc. CoolCon MEECC Conference, 2005: p. 1-83.
21. Zuber, N., *Hydrodynamic Aspects of Boiling Heat Transfer*, in *AEC Report*. 1959.
22. Kutateladze, S.S., *On the Transition to Film. Boiling under Natural Convection.* Kotloturbostroenie, 1948. **3**: p. 10-12.
23. Rosenhow, W.M. and P. Griffith, *Correlation of maximum heat flux data for boiling of saturated liquids.* Chemical Engineering Progress Symposium Series, 1956. **52**(18): p. 47-49.
24. Sadasivan, P., et al., *Possible mechanisms of macrolayer formation.* Int Comm Heat Mass Transfer, 1992. **19**(6): p. 801-805.
25. Bhat, A.M., R. Prakash, and J.S. Saini, *On the mechanism of macrolayer formation in nucleate pool boiling at high heat flux.* International Journal of Heat and Mass Transfer, 1983. **26**(5): p. 735-740.
26. Kandlikar, S.G., *A Theoretical Model to Predict Pool Boiling CHF Incorporating Effects of Contact Angle and Orientation.* J. Heat Transfer, 2001. **123**: p. 1071-1079.

27. Theofanous, T.G. and T.-N. Dinh, *High heat flux boiling and burnout as microphysical phenomena: mounting evidence and opportunities.* Multiphase Sci Technol., 2006. **18**(1): p. 1-26.
28. Gerardi, C.D., *Investigation of the Pool Boiling Heat Transfer Enhancement of Nano-Engineered Fluids by means of High-Speed Infrared Thermography*, in *Department of Nuclear Science and Engineering*. 2009, Massachusetts Institute of Technology: Cambridge. p. 225-235.
29. Dhir, V.K. and S.P. Liaw, *Framework a for unified model for nucleate and transition pool boiling.* Journal Name: Journal of Heat Transfer; (USA); Journal Volume: 111:3, 1989: p. Medium: X; Size: Pages: 739-746.
30. Liter, S.G. and M. Kaviany, *Pool-boiling CHF enhancement by modulated porous-layer coating: theory and experiment* Int. J. Heat Mass Tran., 2001. **44**(22): p. 4287-4311.
31. Guan, C.-K., J.F. Klausner, and R. Mei, *A new mechanistic model for pool boiling CHF on horizontal surfaces.* International Journal of Heat and Mass Transfer, 2011. **54**(17-18): p. 3960–3969.
32. Lin, L. and R. Ponnappan, *Heat transfer characteristics of spray cooling in a closed loop.* International Journal of Heat and Mass Transfer, 2003. **46**(20): p. 3737-3746.
33. Bash, C.E., C.D. Patel, and R.K. Sharma. *Inkjet assisted spray cooling of electronics.* in *International Electronic Packaging Technical Conference and Exhibition (IPACK), Maui, Hawaii.* 2003.
34. Hall, D.D. and I. Mudawar, *Experimental and numerical study of quenching complex-shaped metallic alloys with multiple, overlapping sprays.* International Journal of Heat and Mass Transfer, 1995. **38**(7): p. 1201-1216.
35. Tuckerman, D. and R. Pease, *Optimized Convective Cooling Using Micromachined Structures.* Journal of Electrochemical Society, 1982. **129**(3): p. C98.
36. Triplett, K.A., et al., *Gas-liquid two-phase flow in microchannels - Part I: two-phase flow patterns.* International Journal of Multiphase Flow, 1999. **25**(3): p. 377-394.
37. Triplett, K.A., et al., *Gas-liquid two-phase flow in microchannels - Part II: void fraction and pressure drop.* International Journal of Multiphase Flow, 1999. **25**(3): p. 395-410.
38. Serizawa, A., Z.P. Feng, and Z. Kawara, *Two-phase flow in microchannels.* Experimental Thermal and Fluid Science, 2002. **26**(6-7): p. 703-714.
39. Jiang, L., et al., *Closed-loop electrosmotic microchannel cooling system for VLSI circuits.* IEEE Transactions on Components & Packaging Technologies, 2002. **25**(3): p. 347-355.
40. Penley, S.J. and R.A. Wirtz, *Mechanistic Study of Subatmospheric Pressure, Subcooled, Flow Boiling of Water on Structured-Porous Surfaces.* Journal of Heat Transfer, 2012. **134**(11): p. 112902.
41. Lienhard IV, J.H. and J.H.L. V, *A Heat Transfer Textbook.* 3rd ed. 2008, Cambridge: Phlogiston Press.
42. Lee, P.C., F.G. Tseng, and C. Pan, *Bubble dynamics in microchannels. Part I: single microchannel.* International Journal of Heat and Mass Transfer, 2004. **47**(25): p. 5575–5589.
43. Chang, K.H. and C. Pan, *Two-phase flow instability for boiling in a microchannel heat sink.* International Journal of Heat and Mass Transfer, 2007. **50**(11-12): p. 2078–2088.
44. Kandlikar, S.G., *Fundamental issues related to flow boiling in minichannels and microchannels.* Experimental Thermal and Fluid Science, 2002. **26**(2-4): p. 389–407.
45. Hetsroni, G., et al., *Periodic boiling in parallel micro-channels at low vapor quality.* International Journal of Multiphase Flow, 2006. **32**(10-11): p. 1141–1159.
46. Qu, W. and I. Mudawar, *Measurement and prediction of pressure drop in two-phase microchannel heat sinks.* International Journal of Heat and Mass Transfer, 2003. **46**: p. 2737-2753.
47. Zhang, L., et al., *Phase Change Phenomena in Silicon Microchannels.* International Journal of Heat and Mass Transfer, 2005. **48**(8): p. 1572-1582.
48. Kennedy, J.E., et al., *The onset of flow instability in uniformly heated horizontal microchannels.* Journal of Heat Transfer, 2000. **122**(1): p. 118-125.
49. Koşar, A., C.-J. Kuo, and Y. Peles, *Suppression of Boiling Flow Oscillations in Parallel Microchannels by Inlet Restrictors.* Journal of Heat Transfer, 2006. **128**(3): p. 251-260.

50. Kandlikar, S.G., et al., *Stabilization of Flow Boiling in Microchannels Using Pressure Drop Elements and Fabricated Nucleation Sites.* Journal of Heat Transfer, 2006. **128**: p. 389-396.
51. Koşar, A., C.-J. Kuo, and Y. Peles, *Boiling heat transfer in rectangular microchannels with reentrant cavities.* International Journal of Heat and Mass Transfer, 2005. **48**: p. 4867–4886.
52. Kandlikar, S.G., *Nucleation characteristics and stability considerations during flow boiling in microchannels.* Experimental Thermal and Fluid Science, 2006. **30**: p. 441–447.
53. Krishnamurthy, S. and Y. Peles, *Flow boiling of water in a circular staggered micro-pin fin heat sink.* International Journal of Heat and Mass Transfer, 2008. **51**: p. 1349-1364.
54. Krishnamurthy, S. and Y. Peles, *Flow Boiling Heat Transfer on Micro Pin Fins Entrenched in a Microchannel.* Journal of Heat Transfer, 2010. **132**: p. 041007.
55. Koşar, A. and Y. Peles, *Boiling heat transfer in a hydrofoil-based micro pin fin heat sink.* International Journal of Heat and Mass Transfer, 2007. **50**: p. 1018-1034.
56. Li, D., et al., *Enhancing Flow Boiling Heat Transfer in Microchannels for Thermal Management with Monolithically-Integrated Silicon Nanowires.* Nano Lett., 2012. **12**(7): p. 3385–3390.
57. Kuo, C.-J. and Y. Peles, *Flow Boiling Instabilities in Microchannels and Means for Mitigation by Reentrant Cavities.* Journal of Heat Transfer, 2008. **130**: p. 072402.
58. Nam, Y., et al., *Experimental and Numerical Study of Single Bubble Dynamics on a Hydrophobic Surface.* Journal of Heat Transfer, 2009. **131**(12): p. 121004
59. Nam, Y., et al., *Single Bubble Dynamics on a Superhydrophilic Surface with Artificial Nucleation Sites.* International Journal of Heat and Mass Transfer, 2011. **54**: p. 1572-1577.
60. Chen, R., et al., *Nanowires for Enhanced Boiling Heat Transfer.* Nano Lett., 2009. **9**(2): p. 548-553.
61. Dhir, V.K., *Boiling Heat Transfer.* Annu. Rev. Fluid Mech., 1998. **30**: p. 365–401.
62. Kim, S.J., et al., *Surface wettability change during pool boiling of nanofluids and its effect on critical heat flux.* International Journal of Heat and Mass Transfer, 2007. **50**(19-20): p. 4105-4116.
63. Ahn, H.S., et al., *Effect of liquid spreading due to nano/microstructures on the critical heat flux during pool boiling.* Appl. Phys. Lett., 2011. **98**: p. 071908
64. Betz, A.R., et al., *Do surfaces with mixed hydrophilic and hydrophobic areas enhance pool boiling?* Appl. Phys. Lett., 2010. **97**: p. 141909.
65. Cubaud, T., U. Ulmanella, and C.-M. Ho, *Two-phase flow in microchannels with surface modifications.* Fluid Dynamics Research, 2006. **38**: p. 772-786.
66. Hsu, Y.Y., *On the Size Range of Active Nucleation Cavities on a Heating Surface.* Journal of Heat Transfer, 1961. **84**: p. 207–216.
67. Basu, N., G.R. Warrier, and V.K. Dhir, *Onset of Nucleate Boiling and Active Nucleation Site Density During Subcooled Flow Boiling.* Journal of Heat Transfer, 2002. **124**(717-728).
68. Wang, R., et al., *Light-induced Amphiphilic Surfaces.* Nature, 1997. **388**: p. 431-432.
69. Extrand, C.W., et al., *Superwetting of Structured Surfaces.* Langmuir, 2007. **23**(17): p. 8882–8890.
70. Hiratsuka, K., A. Bohno, and H. Endo, *Water droplet lubrication between hydrophilic and hydrophobic surfaces.* J. Phys.: Conf. Ser., 2007. **89** (1): p. 012012.
71. Öner, D. and T.J. McCarthy, *Ultrahydrophobic Surfaces. Effects of Topography Length Scales on Wettability.* Langmuir, 2000. **16**(20): p. 7777–7782.
72. J. Bico, C. Tordeux, and D. Quéré, *Rough wetting.* Europhysics Letters, 2001. **55**(2): p. 214-220.
73. Seemann, R., et al., *Wetting morphologies at microstructured surfaces.* PNAS, 2004. **102**(6): p. 1848–1852.
74. Martines, E., et al., *Superhydrophobicity and Superhydrophilicity of Regular Nanopatterns.* 5, 2005. **10**(2097–2103).
75. Dupuis, A., et al., *Control of drop positioning using chemical patterning.* Appl. Phys. Lett., 2005. **87**: p. 024103.
76. Gleiche, M., L.F. Chi, and H. Fuchs, *Nanoscopic channel lattices with controlled anisotropic wetting.* Nature, 2000. **403**: p. 173-175.
77. Vorobyev, A.Y. and C. Guo, *Metal pumps liquid uphill.* Appl. Phys. Lett., 2009. **94**: p. 224102.

78. Xiao, R., K.-H. Chu, and E.N. Wang, *Multilayer liquid spreading on superhydrophilic nanostructured surfaces.* Appl. Phys. Lett., 2009. **94**: p. 193104.
79. Courbin, L., et al., *Imbibition by polygonal spreading on microdecorated surfaces.* Nature Materials, 2007. **6**: p. 661 - 664.
80. Zhang, F. and H.Y. Low, *Anisotropic wettability on imprinted hierarchical structures.* Langmuir, 2007. **23**(14): p. 7793–7798.
81. Bico, J., C. Marzolin, and D. Quéré, *Pearl drops.* europhysics Letters, 1999. **47**(2): p. 220-226.
82. Chen, Y., et al., *Anisotropy in the wetting of rough surfaces.* Journal of Colloid and Interface Science, 2005. **281**(2): p. 458–464.
83. Chung, J.Y., J.P. Youngblood, and C.M. Stafford, *Anisotropic wetting on tunable micro-wrinkled surfaces.* Soft Matter, 2007. **3**: p. 1163-1169.
84. Kusumaatmaja, H., et al., *Anisotropic drop morphologies on corrugated surfaces.* Langmuir, 2008. **24**(14): p. 7299-7308.
85. Drelich, J., et al., *Contact angles for liquid drops at a model heterogeneous surface consisting of alternating and parallel hydrophobic/hydrophilic strips.* Langmuir, 1996. **12**(7): p. 1913-1922.
86. Gau, H., et al., *Liquid Morphologies on Structured Surfaces: From Microchannels to Microchips.* Science, 1999. **283**(5398): p. 46-49.
87. Tenhaeff, W.E. and K.K. Gleason, *Initiated and oxidative chemical vapor deposition of polymeric thin films: iCVD and oCVD.* Adv. Funct. Mater., 2008. **18**: p. 979-992.
88. Baxamusa, S.H., S.G. Im, and K.K. Gleason, *Initiated and oxidative chemical vapor deposition: a scalable method for conformal and functional polymer films on real substrates.* PCCP 2009. **11**: p. 5227-5240.
89. Alf, M.E., et al., *Chemical Vapor Deposition (CVD) of conformal, functional, and responsive polymer films.* Adv. Mater., 2009. **21**: p. 1-35.
90. Price, D.C., *A review of selected thermal management solutions for military electronic systems.* IEEE Trans. Compon. Packag. Technol., 2003. **26**(1): p. 26 - 39
91. Kenny, T.W., et al., *Advanced Cooling Technologies for Microprocessorsf.* Int. J. High Speed Electron. Syst, 2006. **16**(1): p. 301-313.
92. Forrest, E., et al., *Augmentation of nucleate boiling heat transfer and critical heat flux using nanoparticle thin-film coatings.* Int. J. Heat Mass Transfer, 2010. **53**: p. 58–67.
93. Li, C.H. and G.P. Peterson, *Experimental study of enhanced nucleate boiling heat transfer on uniform and modulated porous structures.* Front. Heat Transfer, 2010. **1**: p. 023007.
94. Kim, S., et al., *Effects of nano-fluid and surfaces with nano structure on the increase of CHF.* Exp. Therm Fluid Sci., 2010. **34**(4): p. 487–495.
95. Lu, M.-C., et al., *Critical heat flux of pool boiling on Si nanowire array-coated surfaces.* Int. J. Heat Mass Transfer, 2011. **54**(25-26): p. 5359–5367.
96. Li, C., et al., *Nanostructured Copper Interfaces for Enhanced Boiling.* Small, 2008. **4**(8): p. 1084–1088.
97. Theofanous, T.G., et al., *The boiling crisis phenomenon Part I: nucleation and nucleate boiling heat transfer.* Exp. Therm. Fluid Sci., 2002. **26**(6-7): p. 775-792.
98. Xiao, R., R. Enright, and E.N. Wang, *Prediction and Optimization of Liquid Propagation in Micropillar Arrays.* Langmuir, 2010. **26**(19): p. 15070-15075.
99. Gerardi, C., et al., *Infrared thermometry study of nanofluid pool boiling phenomena.* Nanoscale Res. Lett., 2011. **6**: p. 232.
100. Narayan, G.P., K.B. Anoop, and S.K. Das, *Mechanism of enhancement/deterioration of boiling heat transfer using stable nanoparticle suspensions over vertical tubes.* J. Appl. Phys., 2007. **102**: p. 074317.
101. Kim, S.J., et al., *Surface wettability change during pool boiling of nanofluids and its effect on critical heat flux.* Int. J. Heat Mass Transfer, 2007. **50**(19-20): p. 4105-4116.
102. Theofanous, T.G., et al., *The boiling crisis phenomenon Part II: dryout dynamics and burnout.* Exp. Therm. Fluid Sci., 2002. **26**(6-7): p. 793-810.

103. Gerardi, C., et al., *Study of bubble growth in water pool boiling through synchronized, infrared thermometry and high-speed video.* Int. J. Heat Mass Transfer, 2010. **53**(19-20): p. 4185–4192.
104. Han, C.Y. and P. Griffith, *The Mechanism of Heat Transfer in Nucleate Pool Boiling, Part I, Bubble Initiation, Growth and Departure.* Int. J. Heat Mass Tran., 1965. **8**(6): p. 887–904.
105. Rohsenow, W.M., J.P. Hartnett, and E.N. Ganic, *Handbook of heat transfer fundamentals.* 2 ed. 1985, New York: McGraw-Hill.
106. Israelachvili, J.N., *Intermolecular and Surface Forces.* 3 ed. 2011: Elsevier. 432.
107. Lemmon, E.W., M.L. Huber, and M.O. McLinden, *NIST Standard Reference Database 23: Reference Fluid Thermodynamic and Transport Properties-REFPROP, Version 8.0.* 2007, U.S. Department of Commerce, Technology Administration, National Institute of Standards and Technology: Gaithersburg, MD.
108. Takeda, S., et al., *Surface OH group governing adsorption properties of metal oxide films.* Thin Solid Films, 1999. **339** (1-2): p. 220-224.
109. Good, R.J. and E. Ebling, *Generalization of Theory for Estimation of Interfacial Energies.* Industrial & Engineering Chemistry, 1970. **62**(3): p. 54–78.
110. Schiebener, P., et al., *Refractive Index of Water and Steam as Function of Wavelength, Temperature and Density.* J. Phys. Chem. Ref. Data, 1990. **19**(3): p. 677-717.
111. Kanta, A., R. Sedev, and J. Ralston, *Thermally- and Photoinduced Changes in the Water Wettability of Low-Surface-Area Silica and Titania.* Langmuir, 1990. **21**(6): p. 2400-2407.
112. Chu, K.-H., R. Enright, and E.N. Wang, *Microstructured Surfaces for Enhanced Pool Boiling Heat Transfer.* Proceedings of the ASME 2011 International Mechanical Engineering Congress & Exposition, 2011.
113. Chu, K.-H., R. Enright, and E.N. Wang, *Structured surfaces for enhanced pool boiling heat transfer.* Applied Physics Letters, 2012. **100**(24): p. 241603.
114. Tao, Z. and C. Tianhong, *Tunable wetting properties of patterned silicon microchannels with varied surface free energy based on layer-by-layer nano self-assembly.* Journal of Micromechanics and Microengineering, 2011. **21**(4): p. 045015.
115. Joung, Y.S. and C.R. Buie, *Electrophoretic Deposition of Unstable Colloidal Suspensions for Superhydrophobic Surfaces.* Langmuir, 2011. **27**(7): p. 4156-4163.
116. Nam, Y., et al., *Fabrication and Characterization of the Capillary Performance of Superhydrophilic Cu Micropost Arrays.* JMEMS, 2010. **19**(3): p. 581-588.
117. Enright, R., et al., *Condensation on superhydrophobic copper oxide nanostructures.* Journal of Heat Transfer: p. Prepared.
118. *See supplementary material at for the fabrication processes, surface roughness characterization, experimental setup, .*
119. Carey, V.P., *Liquid-Vapor Phase Change Phenomena.* 1992, Bristol: Taylor & Francis.
120. Sangani, A.S. and A. Acrivos, *Slow flow past periodic arrays of cylinders with application to heat transfer.* International Journal of Multiphase Flow, 1982. **8**(3): p. 193–206.
121. Chu, K.-H., R. Xiao, and E.N. Wang, *Uni-directional liquid spreading on asymmetric nanostructured surfaces.* Nature Materials, 2010. **9**: p. 413-417.
122. Wang, E.N., et al., *Droplet mixing using electrically tunable superhydrophobic nanostructured surfaces.* Microfluidics and Nanofluidics, 2009. **7**(1): p. 137-140.
123. Mugele, F. and J.-C. Baret, *Electrowetting: from basics to applications.* J. Phys.: Condens. Matter, 2005. **17**(28): p. 705-773.